

## HARD X-RAY-EMITTING ACTIVE GALACTIC NUCLEI SELECTED BY THE *CHANDRA* MULTIWAVELENGTH PROJECT

J. D. SILVERMAN,<sup>1,2</sup> P. J. GREEN, W. A. BARKHOUSE, D.-W. KIM, T. L. ALDCROFT,  
R. A. CAMERON, B. J. WILKES, A. MOSSMAN, H. GHOSH, AND H. TANANBAUM  
Harvard-Smithsonian Center for Astrophysics, 60 Garden Street, Cambridge, MA 02138;  
jsilverman@cfa.harvard.edu, pgreen@cfa.harvard.edu

M. G. SMITH AND R. C. SMITH  
Cerro Tololo Inter-American Observatory, National Optical Astronomical Observatory, Casilla 603, La Serena, Chile

P. S. SMITH  
Steward Observatory, The University of Arizona, Tucson, AZ 85721

C. FOLTZ  
National Science Foundation, 4201 Wilson Boulevard, Arlington, VA 22230

D. WIK  
Astronomy Department, University of Virginia, P.O. Box 3818, Charlottesville, VA 22903-0818

AND

B. T. JANNUZI  
National Optical Astronomical Observatory, P.O. Box 26732, Tucson, AZ 85726-6732

Received 2004 May 24; accepted 2004 August 29

### ABSTRACT

We present X-ray and optical analysis of 188 active galactic nuclei (AGN) identified from 497 hard X-ray ( $f_{2.0-8.0\text{ keV}} > 2.7 \times 10^{-15}$  ergs cm<sup>-2</sup> s<sup>-1</sup>) sources in 20 *Chandra* fields (1.5 deg<sup>2</sup>) forming part of the *Chandra* Multiwavelength Project. These medium depth X-ray observations enable us to detect a representative subset of those sources responsible for the bulk of the 2–8 keV cosmic X-ray background. Brighter than our optical spectroscopic limit, we achieve a reasonable degree of completeness (77% of X-ray sources with counterparts  $r' < 22.5$  have been classified): broad emission-line AGNs (62%), narrow emission-line galaxies (24%), absorption line galaxies (7%), stars (5%), or clusters (2%). We find that most X-ray unabsorbed AGNs ( $N_{\text{H}} < 10^{22}$  cm<sup>-2</sup>) have optical properties characterized by broad emission lines and blue colors, similar to optically selected quasars from the Sloan Digital Sky Survey but with a slightly broader color distribution. However, we also find a significant population of redder ( $g' - i' > 1.0$ ) AGNs with broad optical emission lines. Most of the X-ray-absorbed AGNs ( $10^{22}$  cm<sup>-2</sup>  $< N_{\text{H}} < 10^{24}$  cm<sup>-2</sup>) are associated with narrow emission-line galaxies, with red optical colors characteristically dominated by luminous, early-type galaxy hosts rather than from dust reddening of an AGN. We also find a number of atypical AGNs; for instance, several luminous AGNs show both strong X-ray absorption ( $N_{\text{H}} > 10^{22}$  cm<sup>-2</sup>) and broad emission lines. Overall, we find that 81% of X-ray-selected AGNs can be easily interpreted in the context of current AGN unification models. Most of the deviations seem to be due to an optical contribution from the host galaxies of the low-luminosity AGNs.

*Subject headings:* galaxies: active — quasars: general — surveys — X-rays: galaxies

*Online material:* color figures, machine-readable table

### 1. INTRODUCTION

In the era of *Chandra* and *XMM-Newton*, X-ray surveys of the extragalactic universe are for the first time able to probe the demographics and evolution of active galactic nuclei (AGNs) irrespective of any moderate obscuration. Current deep surveys such as the CDF-N (Barger et al. 2002), CDF-S (Tozzi et al. 2001), and the Lockman Hole (Mainieri et al. 2002) are unveiling both bright quasars and lower luminosity Seyfert galaxies with significant absorbing gas columns. This obscuration can be large enough to effectively hide any optical signature

of an active nucleus. With the unprecedented sensitivity and resolving power of these current observatories, we are able to probe large volumes to determine the prevalence of X-ray-emitting AGNs and their evolution.

The study of AGNs enshrouded by dust and gas is not new. Obscured AGNs (e.g., narrow-line radio galaxies, Seyfert 2 galaxies, *IRAS* sources) have been under investigation for many years, though a complete census of the population has been out of reach. The spectrum of the cosmic X-ray background (CXRB) has provided evidence of the preponderance of the hidden AGN population. While *ROSAT* has shown that unabsorbed AGNs dominate the soft (0.1–2 keV) CXRB (Hasinger et al. 1998), its high-energy spectrum (2–30 keV) is harder than that of known AGNs. Models based on the CXRB spectrum and the X-ray luminosity function have predicted the existence of large numbers of heavily obscured AGNs that have been missed in past surveys (Comastri et al. 1995; Gilli et al. 2001).

<sup>1</sup> Astronomy Department, University of Virginia, P.O. Box 3818, Charlottesville, VA 22903-0818.

<sup>2</sup> Visiting Astronomer, Kitt Peak National Observatory and Cerro Tololo Inter-American Observatory, National Optical Astronomy Observatory, which is operated by the Association of Universities for Research in Astronomy, Inc. (AURA), under cooperative agreement with the National Science Foundation.

How do these sources fit into the AGN unification scheme (e.g., Antonucci 1993; Antonucci & Miller 1985)? Many of the absorbed X-ray sources lack optical AGN signatures (e.g., Barger et al. 2003). Is this a result of host dilution (Moran et al. 2002) or some other geometry/structure that prevents us from viewing the emission-line gas? While optical extinction and X-ray absorption are statistically correlated (Smith & Done 1996; Turner et al. 1997), there are a number of counterexamples. X-ray observations of Seyfert 2 galaxies do not always provide evidence for a large intrinsic obscuring column (Panessa & Bassani 2002; Georgantopoulos & Zezas 2003). Equally compelling, a number of X-ray–selected type 1 AGNs (Mainieri et al. 2002; Akylas et al. 2003) have significant intrinsic absorption in the X-ray band ( $10^{20} \text{ cm}^{-2} < N_{\text{H}} < 10^{23} \text{ cm}^{-2}$ ). Wilkes et al. (2002) find that a large fraction of the IR-selected AGNs found in the Two-Micron All Sky Survey (2MASS) have broad optical emission lines and a wide range of X-ray absorption. Given the complex environment of some of these AGNs, one line of sight might not always exemplify the overall geometry.

While the *Chandra* and *XMM-Newton* deep fields do cover a large volume, wide-field surveys are needed to compile a significant sample of sources with 2–8 keV flux levels around  $10^{-15}$ – $10^{-14} \text{ ergs cm}^{-2} \text{ s}^{-1}$ . Such sources comprise most of the flux of the 2–8 keV CXRB (Moretti et al. 2003; Cowie et al. 2002). The deep fields provide relatively few sources at these flux levels to characterize the absorbed AGN population. Many ongoing surveys at intermediate flux levels are currently contributing to our understanding of the X-ray–emitting AGNs. For example, the HELLAS2XMM (Fiore et al. 2003) and *XMM-Newton* SSC (Barcons et al. 2003) take advantage of the large field of view and high collecting area of *XMM-Newton*. The SEXSI (Harrison et al. 2003) survey joins the *Chandra* Multiwavelength Project in utilizing *Chandra*’s small PSF and low background to detect the faint AGNs and unambiguously find optical counterparts. With large samples of all AGN types, we can characterize the dominant population contributing to the CXRB and determine the relative importance and nature of interesting AGNs that defy a simple unification model.

## 2. THE *CHANDRA* MULTIWAVELENGTH PROJECT (ChaMP)

The *Chandra* Multiwavelength Project (ChaMP; Kim et al. 2004a, 2004b; Green et al. 2004) is providing a medium-depth, wide-area survey of serendipitous X-ray sources from archival *Chandra* fields covering  $\sim 14 \text{ deg}^2$ . The broadband sensitivity between 0.3–8.0 keV enables the selection to be far less affected by absorption than previous optical, UV, or soft X-ray surveys. *Chandra*’s small point spread function ( $\sim 1''$  resolution on-axis) and low background allow sources to be detected to fainter flux levels, while the  $\sim 1''$  X-ray astrometry greatly facilitates unambiguous optical identification of X-ray counterparts. The project effectively bridges the gap between flux limits achieved with the *Chandra* deep field observations and those of past *ROSAT* and *ASCA* surveys. A total of about 8000 serendipitous extragalactic X-ray sources are expected when the project is complete. A primary aim of the ChaMP is to measure the luminosity function of quasars and lower luminosity AGNs out to  $z \sim 4$  with the inclusion of the obscured population (J. D. Silverman et al. 2004, in preparation).

We present results from the ChaMP using a subsample ( $f_{2-8 \text{ keV}} > 2.7 \times 10^{-15} \text{ ergs cm}^{-2} \text{ s}^{-1}$  and  $r' < 22.5$ ) of 497 X-ray sources detected in the hard band (2.5–8.0 keV) in 20

fields. This work is an extension of the six fields analyzed by Green et al. (2004), here limited to the hard X-ray band. From this subsample, we classify 188 as AGNs based on their X-ray luminosity ( $L_{2-8 \text{ keV}} > 10^{42} \text{ ergs s}^{-1}$ ). Our motivation is to determine the demographics of the hard X-ray–emitting AGNs, measure the range of intrinsic obscuration, and determine the extent to which obscuration of X-rays translates to extinction in the optical. After briefly discussing the X-ray and optical data acquisition, reduction and analysis (§§ 3 and 4), we describe the characteristics of the hard X-ray sources (§ 5) and the AGN properties (§ 6) including selection and completeness. In § 7, we present the results. Throughout this paper, we assume  $H_0 = 70 \text{ km s}^{-1} \text{ Mpc}^{-1}$ ,  $\Omega_{\Lambda} = 0.7$ , and  $\Omega_M = 0.3$ .

## 3. X-RAY OBSERVATIONS

We have chosen 20 *Chandra* fields (Table 1) for which we have acquired extensive follow-up optical imaging and spectroscopy. These fields have been selected from the first 2 years of *Chandra* archival data. Only ACIS observations at high Galactic latitude ( $|b| > 20^\circ$ ) with no special observing modes (e.g., gratings) are used. The deepest observations have exposure times that are sensitive to sources with  $f_{2-8 \text{ keV}} > 2 \times 10^{-15} \text{ ergs cm}^{-2} \text{ s}^{-1}$ . At this flux limit, we resolve  $\sim 70\%$  of the 2–8 keV CXRB (Moretti et al. 2003; Fig. 5). The target of each observation has been excluded to avoid any bias toward specific objects such as AGNs associated with clusters.

A full description of the ChaMP image reduction and analysis pipeline XPIPE can be found in Kim et al. (2004a). In short, we have an automated reduction routine that filters out high background intervals, bad events such as cosmic rays and hot pixels to produce a clean and robust X-ray source catalog. Source extraction is performed using a wavelet detection algorithm (CIAO wavdetect; Freeman et al. 2002) in three energy bands [broad (B), 0.3–8.0 keV; soft (S), 0.3–2.5 keV; hard (H), 2.5–8.0 keV].

For the following analysis, we require a S/N  $> 2$  in the 2.5–8.0 keV band to generate a hard X-ray–selected sample that minimizes any inherent bias against the absorption of soft X-rays. We restrict the off-axis angle of the detections to less than  $12'$  since the sensitivity beyond this is significantly reduced. We do not use chip S4 (ccd\_id = 8) since this CCD is severely affected by a flaw in the serial readout, causing a significant amount of charge to be randomly deposited along pixel rows as they are read out. Each detection has a unique effective exposure time that includes vignetting. The conversion from X-ray count rate to flux units ( $\text{ergs cm}^{-2} \text{ s}^{-1}$ ) is determined from simulated detections on each CCD of a source with a power-law spectrum ( $f_E \propto E^{-(\Gamma-1)}$ ;  $\Gamma = 1.7^3$ ) and Galactic absorption (Dickey & Lockman 1990). The effect of varying the photon index ( $\Gamma$ ) from 1.7 to 1.9 results in a  $\sim 2\%$  difference in flux for both ACIS-I and ACIS-S. We calculate the flux in the conventional 2.0–8.0 keV band for comparison with other surveys.

With *Chandra*’s broadband sensitivity (0.3–8.0 keV), we are able to investigate the spectral properties of the sample, though we are limited by the small number of source counts in most cases (90% of sources have  $9 < \text{counts} < 70$  in the 2.0–8.0 keV band). The hardness ratio (HR = H – S/H + S) can be used as a crude assessment of the spectral characteristics. Since the response of *Chandra* varies as a function of energy and off-axis angle with the additional complication of mixing frontside- and

<sup>3</sup> The ChaMP XPIPE (Kim et al. 2004a) provides energy conversion factors (ECF) for two models with  $\Gamma = 1.7$  and  $\Gamma = 1.4$ . We chose the former since the photon index more closely resembles the majority of the hard source detections.

TABLE 1  
*Chandra* FIELDS

Obs. ID	PI Target	Exposure <sup>a</sup> (ks)	ACIS CCDs <sup>b</sup>	R.A. (J2000) <sup>c</sup>	Decl. (J2000) <sup>c</sup>	UT Date	Galactic $N_{\text{H}}^{\text{d}}$ ( $10^{20} \text{ cm}^{-2}$ )
520.....	MS 0015.9+1609	61.0	0123	00 18 33.4	+16 26 34.8	2000 Aug 18	4.06
913.....	CL J0152.7–1357	34.6	012367	01 52 43.0	–13 57 30.0	2000 Sep 08	1.61
796.....	SBS 0335–052	47.0	0123	03 37 44.0	–05 02 39.0	2000 Sep 07	4.98
624.....	LP 944–20	40.9	2367	03 39 34.7	–35 25 50.0	1999 Dec 15	1.44
902.....	MS 0451.6–0305	41.5	2367	04 54 10.9	–03 01 07.2	2000 Oct 08	5.18
914.....	CL J0542–4100	48.7	0123	05 42 50.2	–41 00 06.9	2000 Jul 26	3.59
1602.....	Q0615+820	43.1	2367	06 26 02.9	+82 02 25.5	2001 Oct 18	5.27
377.....	B2 0738+313	26.9	367	07 41 10.7	+31 12 00.4	2000 Oct 10	4.18
2130.....	3C 207	30.0	2367	08 40 48.0	+13 12 23.0	2000 Nov 04	4.14
512.....	EMSS 1054.5–0321	75.6	2367	10 57 00	–03 37 00.0	2000 Apr 21	3.67
536.....	MS 1137.5+6625	114.6	0123	11 40 23.3	+66 08 42.0	1999 Sep 30	1.18
809.....	Mrk 273X	40.9	2367	13 44 47.5	+55 54 10.0	2000 Apr 19	1.09
541.....	V1416+4446	29.8	0123	14 16 28.8	+44 46 40.8	1999 Dec 02	1.24
548.....	RX J1716.9+6708	50.3	0123	17 16 52.3	+67 08 31.2	2000 Feb 27	3.71
830.....	Jet of 3C 390.3	23.6	2367	18 41 48.1	+79 47 43.0	2000 Apr 17	4.16
551.....	MS 2053.7–0449	42.3	01236	20 56 22.2	–04 37 44.4	2000 May 13	4.96
928.....	MS 2137–2340	29.1	2367	21 40 12.7	–23 39 27.0	1999 Nov 18	3.57
431.....	Einstein Cross	21.9	2367	22 40 30.4	+03 21 31.0	2000 Sep 06	5.34
918.....	CL J2302.8+0844	106.1	0123	23 02 48.1	+08 44 00.0	2000 Aug 05	5.50
861.....	Q2345+007	65.0	267	23 48 19.6	+00 57 21.1	2000 Jun 27	3.81

<sup>a</sup> Effective screened exposure time for the on-axis chip.

<sup>b</sup> The ACIS CCD chips used in the observation with the aim point chip underlined. CCD 8 has been excluded (see text).

<sup>c</sup> Nominal target position, not including any *Chandra* pointing offsets. Units of right ascension are hours, minutes, and seconds, and units of declination are degrees, arcminutes, and arcseconds.

<sup>d</sup> Galactic column density taken from Dickey & Lockman (1990).

backside-illuminated CCDs, we have converted the raw HR to an effective, on-axis, ACIS-I value by multiplying the count rate in each band by the ratio of the ECF (off-axis CCD) to the on-axis ECF, which ranges between 0.6 and 2.0.

### 3.1. X-Ray Spectral Fits

X-ray spectral modeling provides a robust way of characterizing the spectral properties of our sample, independent of observation and instrument details. With a measured redshift, we can more accurately determine the intrinsic absorbing column than that based solely on hardness ratios. Some objects that look soft in HR may have significant absorption especially at higher redshifts. For each X-ray source in our hard-selected sample, we use an automated procedure to extract the spectrum and fit a model to the data. Owing to a lack of counts, we cannot usefully fit a spectral power-law model, leaving both spectral index and intrinsic absorbing column free for all objects.

All processing is done using CIAO 3.0.2<sup>4</sup> and CALDB 2.26.<sup>5</sup> The detailed steps to prepare the PHA (pulse-height analysis) spectrum follow. First, we define a circular region centered on the X-ray source sized to contain 95% of 1.5 keV photons at the given off-axis angle. The background region is annular with a width of 20'' centered on the source. We exclude any nearby sources from both the source and background regions. We then use CIAO tool “psextract” to create a PHA spectrum covering the energy range 0.4–8 keV. We generate both an ungrouped spectrum and one that is grouped to a minimum of 10 counts per channel. The time-dependent quantum efficiency degradation of ACIS is accounted for when the ARF is generated by the “mkarf” tool.

Spectral fitting is done using the CIAO *Sherpa*<sup>6</sup> tool. For all sources, we fit an absorbed power law containing an intrinsic absorber with neutral column  $N_{\text{H}}$  at the source redshift. Our choice of photon index (Frozen at  $\Gamma = 1.9$ ) is based on previous studies of unabsorbed AGNs. Reeves & Turner (2000) have measured the spectral index for radio-quiet AGNs using *ASCA* observations to be  $\Gamma \sim 1.9$ . Piconcelli et al. (2003) have measured a mean photon index 1.8–1.9 with *XMM-Newton* that shows no variation over the redshift range  $0 < z < 2$ . This  $N_{\text{H}}$  fit provides a robust one-parameter characterization of the intrinsic spectral shape for as few as 10 counts. We verified by an extensive Monte Carlo simulation that the parameter uncertainties calculated with *projection* of confidence contours in *Sherpa* are reliable. Note that the spectral model contains a fixed Galactic neutral absorber appropriate for each object. Spectra with at least 60 counts are fitted using the grouped spectrum with the hybrid Monte Carlo Levenberg-Marquardt minimization method, while the low count spectra are fitted using the ungrouped data with Cash statistics and the Powell method. Spectra with over 200 counts are also fitted with a two-parameter absorbed power law leaving both  $\Gamma$  and the intrinsic  $N_{\text{H}}$  at the source redshift free to vary. The results from the two-parameter fitting are included in this paper for a couple of sources discussed in § 7.2. The full analysis will be presented in an upcoming ChaMP paper (T. L. Aldcroft et al. 2004, in preparation).

## 4. OPTICAL FOLLOW-UP

### 4.1. Imaging

We have acquired optical imaging for each *Chandra* field to identify counterparts to X-ray sources. We use the NOAO

<sup>4</sup> See <http://cxc.harvard.edu/ciao>.

<sup>5</sup> See <http://cxc.harvard.edu/caldb>.

<sup>6</sup> See <http://cxc.harvard.edu/sherpa>.

TABLE 2  
KPNO 4 m OPTICAL IMAGING

Obs. ID	UT Date	Filter	Dithers	Exposure (Total s)	Air Mass (Mean)	FWHM <sup>a</sup> (arcsec)	$m_{TO}^b$ Limit	$m_{5\sigma}^c$ Limit
377.....	2001 Feb 21	<i>g'</i>	3	1800	1.00	1.1	25.4	26.5
		<i>r'</i>	3	1500	1.01	1.0	24.9	26.0
		<i>i'</i>	3	1500	1.04	1.1	24.1	25.2
431.....	2000 Jun 11	<i>g'</i>	2	1000	1.36	1.6	24.1	25.4
		<i>r'</i>	1	500	1.28	1.6	23.4	24.7
		<i>i'</i>	1	360	1.25	1.2	22.9	24.1
512.....	2001 Feb 21–22	<i>g'</i>	5	4500	1.29	1.3	24.9	26.3
		<i>r'</i>	3	2400	1.23	1.1	24.4	25.8
		<i>i'</i>	5	2000	1.29	1.3	23.6	24.8
520.....	2001 Oct 25	<i>g'</i>	3	1950	1.24	1.2	24.1	25.2
		<i>r'</i>	3	1200	1.34	1.2	23.9	24.9
		<i>i'</i>	3	900	1.46	1.4	22.6	24.0
548.....	2000 Jun 10	<i>g'</i>	2	1800	1.28	1.2	24.8	26.2
		<i>r'</i>	2	1200	1.24	1.3	24.1	25.4
		<i>i'</i>	2	1200	1.22	1.7	23.4	24.6
551.....	2000 Jun 10, 12	<i>g'</i>	3	2100	1.28	1.7	24.4	25.6
		<i>r'</i>	4	1200	1.25	1.8	23.9	25.0
		<i>i'</i>	2	600	1.24	1.4	22.9	24.5
796.....	2001 Oct 24	<i>g'</i>	3	2700	1.33	1.1	25.1	26.4
		<i>r'</i>	3	2400	1.52	1.2	24.6	25.7
		<i>i'</i>	3	1200	1.28	1.1	23.6	24.8
809.....	2000 Jun 11	<i>g'</i>	3	2100	1.19	1.8	23.1	24.4
		<i>r'</i>	3	1500	1.14	1.7	23.4	24.6
		<i>i'</i>	3	1500	1.10	1.8	23.1	24.4
830.....	2000 Jun 11	<i>g'</i>	3	1800	1.49	1.6	24.1	25.6
		<i>r'</i>	2	1000	1.49	1.6	23.4	24.8
		<i>i'</i>	1	600	1.49	1.6	22.9	24.2
902.....	2001 Oct 23	<i>g'</i>	3	1800	1.24	1.0	24.9	26.2
		<i>r'</i>	3	1800	1.22	1.1	24.4	25.6
		<i>i'</i>	3	1200	1.24	1.0	23.6	24.9
913.....	2001 Oct 23	<i>g'</i>	5	3500	1.46	1.1	25.1	26.4
		<i>r'</i>	5	3000	1.44	1.0	24.6	25.9
		<i>i'</i>	5	2000	1.52	1.1	23.6	24.8
918.....	2001 Oct 23	<i>g'</i>	5	4500	1.20	1.2	24.9	26.0
		<i>r'</i>	5	3000	1.09	1.3	24.1	25.6
		<i>i'</i>	5	1500	1.12	1.2	23.1	24.8
1602.....	2001 Dec 14	<i>g'</i>	1	520	1.56	2.4	23.3	24.8
		<i>r'</i>	3	1800	1.56	2.1	23.1	24.8
		<i>i'</i>	3	1800	1.56	2.5	22.6	24.7
2130.....	2001 Feb 22	<i>g'</i>	3	3000	1.16	1.4	25.1	26.5
		<i>r'</i>	3	2700	1.08	1.3	24.9	25.9
		<i>i'</i>	5	2500	1.06	0.9	24.6	25.8

NOTE.—We tabulated 14 additional ChaMP fields following Green et al. (2004).

<sup>a</sup> FWHM of point sources in final stacked images.

<sup>b</sup> Turnover magnitude limit at  $\sim 90\%$  completeness, using 0.25 mag bins before extinction correction, as described in the text.

<sup>c</sup> Magnitude limit for a  $\sim 5\sigma$  detection.

Blanco and Mayall 4 m telescopes and their MOSAIC cameras to image the full *Chandra* field of view of our survey fields. The exposure times are scaled from the minimum X-ray flux for a detection per *Chandra* field to identify more than 90% of *ROSAT* AGNs (Yuan et al. 1998). Three filters (*g'*, *r'*, *i'*) using the Sloan Digital Sky Survey (SDSS) photometric system (Fukugita et al. 1996) are implemented to measure broadband colors for preliminary source classification. Table 2 provides some details of the imaging for the 14 fields not included in Green et al. (2004).

A full description of the optical follow-up program including strategy, image reduction, source detection, and photometric calibration can be found in (Green et al. 2004). Briefly, optical image reduction on the MOSAIC data is performed with the

“mscred” (Valdes 2002) package within the IRAF<sup>7</sup> environment. We use the SExtractor (Bertin & Arnouts 1996) algorithm to detect sources, and measure their positions and brightness. Since the X-ray source positions are only accurate to within  $\sim 1''$ , the optical astrometric solution is required to achieve the rms  $< 0''.3$  accuracy necessary for spectroscopic follow-up. We require an accuracy of the photometric solution to less than a tenth of a magnitude. The majority of the AGN sample (88%) presented in this paper has magnitude errors of less than 0.05 as

<sup>7</sup> IRAF is distributed by the National Optical Astronomy Observatory, which is operated by the Association of Universities for Research in Astronomy, Inc., under cooperative agreement with the National Science Foundation.

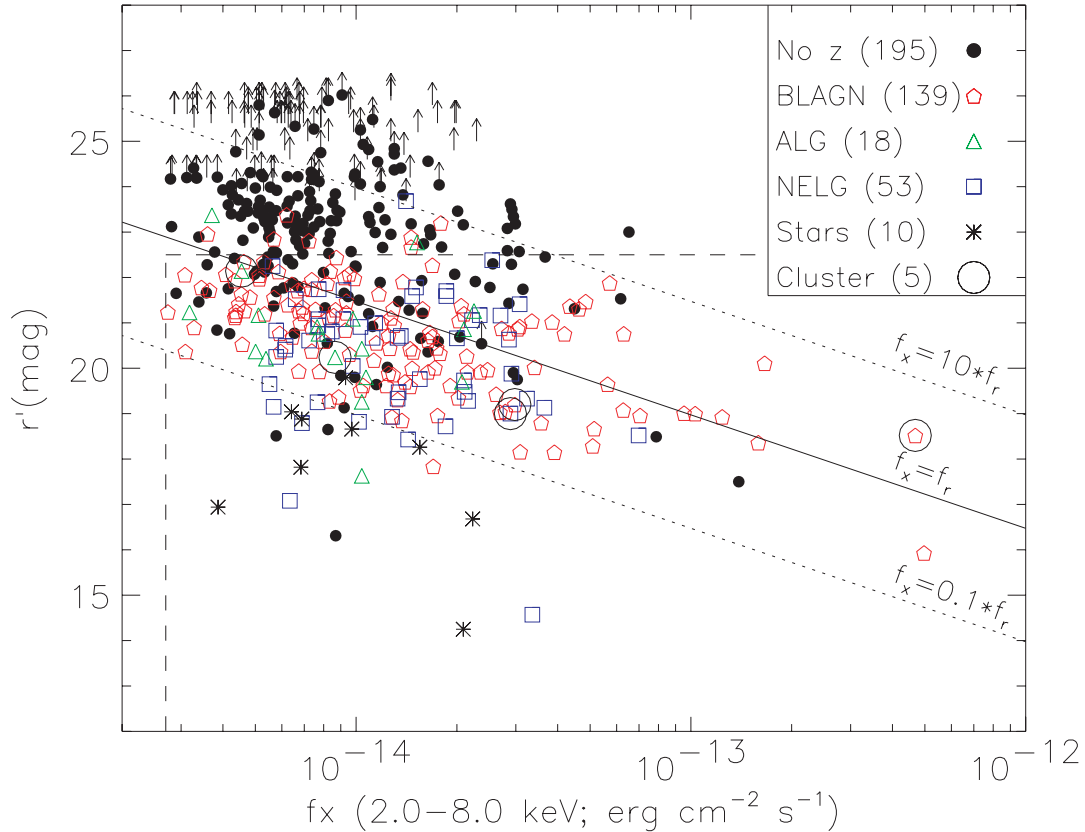


FIG. 1.—X-ray flux (2–8 keV) vs. optical magnitude ( $r'$ ). Optical spectroscopic classifications are indicated (*top right box*) with the sample size in parenthesis. X-ray sources with no optical counterparts are shown by an arrow placed at the hypothetical magnitude for a  $5\sigma$  detection from our optical imaging (Table 2). The dashed vertical and horizontal lines mark the X-ray flux limit and optical magnitude limit for the subsequent analysis. The slanted lines mark the  $f_x/f_r$  ratios of 0.1, 1, and 10.

a result of the bright optical magnitude selection. In addition, we find a mean color offset of 0.05 mag to the red between our  $g' - i'$  color and the SDSS using sources detected in both surveys.

#### 4.2. X-Ray-to-Optical Source Matching

We implement an automated routine to match each X-ray source with potential optical counterparts (see Green et al. 2004). The search radius is increased for X-ray detections at large off-axis angles. Each match is visually inspected and a confidence level is determined. For X-ray sources with multiple optical counterparts, the optical source closest to the X-ray centroid is usually given a higher confidence. We have found 415 optical counterparts to 497 X-ray sources (84%; Fig. 1). We have not included 36 sources because the X-ray detection fell on a chip edge or there were multiple optical counterparts for which no single optical source could confidently be assigned. We note that 81% of the matches have an X-ray to optical offset of less than  $2''$ .

#### 4.3. Spectroscopy

Optical spectroscopy is crucial for determining the source type and redshift. We acquired the majority of our optical spectra with the WIYN 3.5 m and CTIO 4 m with the HYDRA multifiber spectrographs, which have a field of view ( $>40'$ ) that fully covers the *Chandra* field. To extend spectroscopic classifications beyond  $r' \sim 21$ , the limit of the 4 m class telescopes with HYDRA, we have obtained spectra from Magellan and the MMT. The field of view of Magellan with LDSS-2, a multislit

spectrograph, is  $5'$ , so it takes 5–6 pointings to cover the full *Chandra* field. We have been using the FLWO 1.5 m to acquire spectra of the optically bright ( $r' < 17$ ) counterparts. In addition, a number of people, mentioned in the acknowledgements, have graciously acquired long-slit spectra of a few ChaMP sources during their own observing time. All redshifts have an accuracy of  $\Delta z < 0.001$ . Table 3 gives a summary of the spectroscopic facilities used by the ChaMP project.

We implement a classification scheme of optical spectra similar to the *Einstein Observatory* Extended Medium-Sensitivity Survey (Stocke et al. 1991). Objects with strong emission lines ( $W_\lambda > 5 \text{ \AA}$ ) are classified as either broad-line AGNs (BLAGNs;  $\text{FWHM} > 1000 \text{ km s}^{-1}$ ) or narrow emission-line galaxies (NELGs;  $\text{FWHM} < 1000 \text{ km s}^{-1}$ ). Counterparts with weak emission line or pure absorption line spectra are classified as absorption line galaxies (ALGs). We note that there is a combination of redshift range and spectral bandpass for which we may lose important AGN optical diagnostic features. In some cases, the host galaxy contribution can prevent  $H\beta$  from being a useful AGN indicator. Given the low signal-to-noise of our spectra, some NELGs may have weak, broad emission lines. Ho et al. (1997) found that broad  $H\alpha$  can often be found in low-luminosity “dwarf” Seyferts with high S/N spectra and proper subtraction of the stellar continuum. This type of analysis is not possible given the quality of our spectra. Any stellar source is labeled as a STAR. For the ALGs, we measure the Ca II break “CONTRAST” (Stocke et al. 1991) to look for a power-law AGN component to the continuum to note potential BL Lac candidates. If the associated X-ray emission is extended, the object is further labeled as a possible cluster member.

TABLE 3  
OPTICAL SPECTROSCOPIC FOLLOW-UP

Telescope	Instrument	Grating/Grism	$\lambda$ Range (Å)	$R$ ( $\lambda/\Delta\lambda$ )	Spectral Resolution (Å)	Number of Spectra
WIYN <sup>a</sup> .....	HYDRA	316 at 7.0	4500–9000	950	7.8	91
CTIO 4 m .....	HYDRA	KPGL3	4600–7400	1300	4.6	48
Magellan.....	LDSS-2	Med. red and blue	3600–8500 <sup>b</sup>	520	13.5	41
Magellan.....	B&C	300 lines mm <sup>-1</sup>	3700–8700	384	13.0	7
MMT.....	Blue Channel	300 lines mm <sup>-1</sup>	3500–8300	800	8.8	15
Keck I.....	LRIS	300/5000	4000–9000	484	13	5
FLWO 1.5 m.....	FAST	300 lines mm <sup>-1</sup>	3600–7500	850	5.9	2

<sup>a</sup> The WIYN Observatory is a joint facility of the University of Wisconsin Madison, Indiana University, Yale University, and the National Optical Astronomy Observatory.

<sup>b</sup> Spectral coverage can vary as a function of slit position in the mask.

As shown in Figure 1, we have classified 44% (220) of all the hard X-ray sources through our spectroscopic campaign. The sources without redshifts are primarily at faint optical magnitudes ( $r' > 22$ ). In Table 5, we list the numbers of each type for various limits imposed on the sample.

## 5. CHARACTERISTICS OF THE HARD X-RAY SAMPLE

### 5.1. X-Ray and Optical Flux

We show the optical magnitude ( $r'$ ) as a function of X-ray flux (2.0–8.0 keV) for the 497 sources detected in 20 fields (Fig. 1). Lines of constant  $f_x/f_{r'}$  are determined as follows:

$$\log(f_x/f_{r'}) = \log(f_x) + 0.4r' + 5.41. \quad (1)$$

This relation has been derived using an assumed power law ( $f_E \propto E^{-\alpha}$ ) with spectral index  $\alpha_o = 0.5$  and  $\alpha_x = 0.7$ . The characteristics of the  $r'$  filter are taken from Fukugita et al. (1996). Most objects have  $0.1 < f_x/f_{r'} < 10$ . There exists a significant number of X-ray–bright, optically faint sources ( $f_x/f_{r'} > 10$ ), many of which are not detected in our optical imaging. Owing to their optical faintness, we have only identified one such source, an NELG.

Based on the 210 spectroscopically identified objects with  $r' < 22.5$ , we find that 62% of the hard X-ray sources are classified as BLAGN. As shown in Green et al. (2004), these AGNs tend to follow the relation  $f_x = f_{r'}$  over a wide range of optical and X-ray flux. The NELGs, which comprise 24% of the identifications, have flux ratios similar to the BLAGNs. We find a number of counterparts (7% ALGs) that have no evidence for an emitting line region. These galaxies are primarily identified at bright optical magnitudes ( $r' < 21$ ) because of the difficulty of classifying sources without strong emission lines at high redshift ( $z > 0.5$ ). In addition, a few hard X-ray–detected sources are associated with optically bright stars (5%) and galaxy clusters (2%) with extended X-ray emission.

### 5.2. X-Ray Spectral Properties

The X-ray hardness ratio provides a crude measure of the spectral properties and classification of the hard X-ray sources. In Figure 2, we plot the corrected hardness ratio (§ 3) as a function of X-ray flux. The flux range shown includes all sources with the exception of the extremely bright cataclysmic variable TX Col (Schlegel & Salinas 2004). The horizontal lines mark the hardness ratio, which corresponds to an X-ray source with a power-law continuum (photon index  $\Gamma = 1.9$ )

absorbed by a column of gas at  $z = 0$ . Some of the derived  $N_{\text{H}}$  detections may be higher (see § 3.1) using an absorber intrinsic to the source. According to Moretti et al. (2003), we are resolving  $\sim 70\%$  of the full 2–8 keV CXRB at our chosen flux limit. With a flux-weighted mean HR for the ChaMP sources of  $-0.39$ , the X-ray spectrum of the ensemble is similar to the spectral characteristic of the integrated CXRB ( $\Gamma = 1.4$ ), which corresponds to a hardness ratio of  $-0.42$ .

As described in many studies with *Chandra* (e.g., Mushotzky et al. 2000) and *XMM-Newton* (e.g., Hasinger et al. 2001), the X-ray source population becomes relatively harder at fainter flux levels. As evident in Figure 2, the hardest (HR  $> 0$ ) X-ray sources in these ChaMP fields are predominately at  $\log_{10}(f_x) < -13.6$ . At fainter flux levels, the sources have a more even distribution over all hardness ratios. This spectral variation has been attributed to intrinsic absorption rather than changes in the intrinsic spectral energy distribution (Mainieri et al. 2002; Kim et al. 2004b). This will be further investigated in an upcoming ChaMP paper on the X-ray spectral properties of the AGN sample.

## 6. HARD AGN SAMPLE

### 6.1. Selection and Completeness

In these medium depth *Chandra* fields, we are sensitive to X-ray sources with a 2.0–8.0 keV flux greater than  $2.7 \times 10^{-15}$  ergs  $\text{cm}^{-2}$   $\text{s}^{-1}$ . The addition of a spectroscopic limit of  $r' < 22.5$ , yields a sample of X-ray sources that is 77% identified. This optical magnitude limit does bias the sample against optically faint counterparts at the lower X-ray flux levels.

To construct a pure AGN sample, we require the rest-frame 2.0–8.0 keV luminosity (uncorrected for intrinsic absorption) to exceed  $10^{42}$  ergs  $\text{s}^{-1}$  thereby excluding any sources that may contain a significant stellar or hot ISM component. The most luminous known star-forming (Zezas et al. 2003; Lira et al. 2002) or elliptical (O’Sullivan et al. 2001) galaxies attain at most  $L_X = 10^{42}$  ergs  $\text{s}^{-1}$ . Since many of the traditional optical AGN signatures are not present in obscured sources, high X-ray luminosity becomes our single discriminant for supermassive black hole accretion. We believe that almost all of the NELGs and ALGs harbor accreting SMBHs based on their X-ray luminosity. We find that 90% of the identified ChaMP sources have luminosities above this threshold. These selection criteria yield a sample of 188 AGNs from 20 *Chandra* fields with  $f_{2-8 \text{ keV}} > 2.7 \times 10^{-15}$  ergs  $\text{cm}^{-2}$   $\text{s}^{-1}$ ,  $r' < 22.5$ , and  $L_X > 10^{42}$  ergs  $\text{s}^{-1}$ . We have removed five objects identified as clusters based on their extended X-ray emission. A truncated version of the AGN

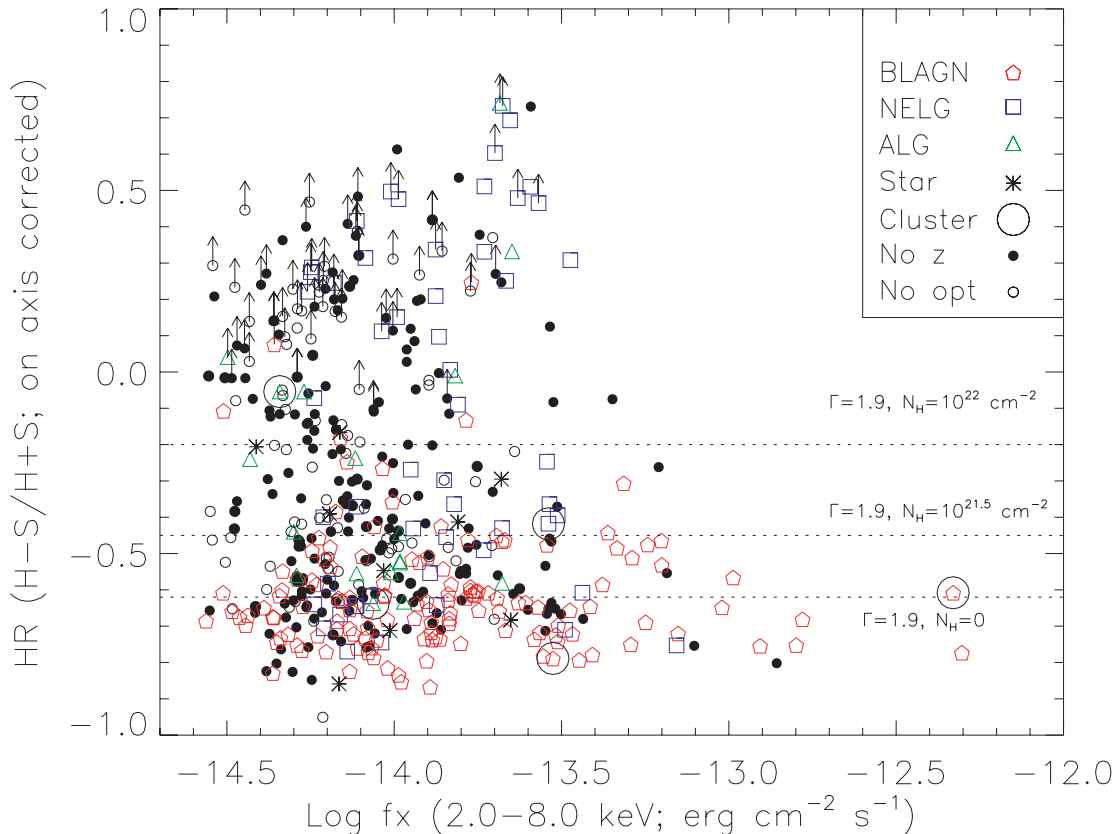


FIG. 2.—X-ray hardness ratio (HR) as a function of 2.0–8.0 keV flux. The hardness ratio has been recalculated to the equivalent on-axis value for all sources. Error bars have been omitted for clarity and lower limits are marked by an arrow. Symbol type indicates the spectroscopic classification. Objects with no spectrum are marked as filled circles, while objects with no optical counterpart are marked by a small open circle.

catalog is presented in Table 4. This sample is composed of 69% BLAGNs, 24% NELGs, and 7% ALGs (Table 5).

### 6.2. Redshift and Luminosity Distribution

As shown in Figure 3, *Chandra* detects hard BLAGNs out to  $z \sim 4$  in these medium depth observations. In contrast, we have only identified non-BLAGNs with  $z < 0.8$ . The steep drop in the number of NELGs and ALGs above this redshift is primarily due to an optical selection bias. The NELGs and ALGs lack prominent broad emission lines and may be resolved, having a magnitude fainter than our  $r' = 22.5$  limit within our spectroscopic aperture. Even a luminous host galaxy ( $10L_*$ ) at  $z \sim 0.8$  is fainter than this limit. However, the *Chandra* Deep field surveys are finding a peak in the number distribution at  $z \sim 0.8$  with a sharp drop-off beyond  $z \sim 1$  (Cowie et al. 2003). Therefore, the peak in our distribution for NELGs and ALGs is unlikely to change drastically with the identification of the optically faint sources.

### 6.3. Low-Luminosity AGNs and Composite Systems

Even though we have mitigated bias against obscured AGNs by carrying out a hard X-ray survey, we still need to incorporate the optical properties of these AGNs to determine their nature and how they fit into the unification scheme. Many of the newly detected *Chandra* and *XMM-Newton* sources in the deep fields show no evidence for an AGN in the optical.

Optical emission from these low-luminosity AGNs can include a significant contribution from the host galaxy (Fiore et al. 2003; Green et al. 2004). This tends to be the case for AGNs with  $L_X < 10^{43}$  ergs  $s^{-1}$ . We plot in Figure 4 the mono-

chromatic, rest-frame optical (2500 Å) versus X-ray (2 keV) luminosity density for our hard AGN sample with  $f_{2-8 \text{ keV}} > 1 \times 10^{-14}$  ergs  $cm^{-2} s^{-1}$  and  $r' < 22.5$ . We measure the optical luminosity density at 2500 Å from the  $r'$  magnitude as in Fukugita et al. (1996), assuming a power-law spectrum with  $\alpha_o = 0.5$ . The monochromatic X-ray luminosity is derived from the hard-band flux using a power-law spectrum with  $\alpha_x = 1.0$ . The additional X-ray flux limit is imposed to include BLAGNs across the full range of  $\alpha_{ox}$  ( $\sim 1-2$ ). If we included BLAGNs with fainter X-ray fluxes, we would be biasing the sample too strongly toward optically bright objects based on our optical magnitude limit. The BLAGNs above  $\log \nu_{l, (2.0 \text{ keV})} > 43.5$  share a similar X-ray-to-optical ratio ( $\langle \alpha_{ox} \rangle = 1.48 \pm 0.03$ ), while the lower luminosity AGNs depart from this relation.

Most studies of X-ray-selected AGNs rely on optical spectroscopy for further classification. This can be misleading since it is difficult to isolate the nuclear region at these distances (Moran et al. 2002) with a  $\sim 1''$  aperture. While most of the optical counterparts of *Chandra* sources have emission lines similar to quasars and lower luminosity Seyfert galaxies, limited wavelength coverage can cause some confusion with source classification as described by Page et al. (2003). For example, we display in Figure 5 two sources each with optical spectra spanning different wavelength ranges. Depending on the observed wavelength coverage, the classification can change drastically with the detection of broad emission lines either at the blue end of the spectrum (source 35; Mg II) or the red end (source 42; H $\alpha$ ). However, the inclusion of these AGNs in our sample highlight the power of X-ray selection to reveal supermassive black hole accretion even under a veil of obscuration or host contamination.

TABLE 4  
HARD AGNs

Source Number	ChaMP Name	R.A. (J2000)	Decl. (J2000)	Hard <sup>a</sup> Counts	$\log f_x^b$	HR	$z$	$\log L_x^c$	$r'$	$g' - i'$	$r' - i'$	Class	$\log N_H$ (cm <sup>-2</sup> )
1.....	CXOMP J001845.7+163346	00 18 45.74	+16 33 46.6	89.0 ± 10.7	-13.51	-0.40	0.624	43.70	21.41	1.58	0.66	NELG	21.89 <sup>+0.15</sup> <sub>-0.18</sub>
2.....	CXOMP J001837.3+163447	00 18 37.38	+16 34 47.1	18.4 ± 5.8	-14.17	-0.71	2.149	44.37	19.94	0.23	0.15	BLAGN	<21.61
3.....	CXOMP J001833.4+163154	00 18 33.47	+16 31 54.4	38.0 ± 7.3	-13.90	-0.65	1.643	44.36	21.11	0.73	0.39	BLAGN	<21.58
4.....	CXOMP J001837.4+163757	00 18 37.48	+16 37 57.7	19.5 ± 7.3	-14.13	-0.71	1.506	44.03	20.90	0.45	0.16	BLAGN	<22.35
5.....	CXOMP J001828.6+163418	00 18 28.68	+16 34 18.2	9.0 ± 4.4	-14.48	-0.66	1.163	43.40	20.90	0.38	0.04	BLAGN	<21.97
6.....	CXOMP J001842.0+163425	00 18 42.09	+16 34 25.0	9.3 ± 4.6	-14.50	>0.04	0.550	42.59	21.23	2.66	0.82	ALG	<22.14
7.....	CXOMP J001825.0+163653	00 18 25.01	+16 36 53.0	15.6 ± 6.1	-14.25	-0.49	1.198	43.67	21.56	<-2.07	<-2.47	BLAGN	<22.28
8.....	CXOMP J001850.1+162756	00 18 50.14	+16 27 56.4	20.5 ± 5.9	-14.16	-0.63	1.330	43.87	21.21	0.35	-0.06	BLAGN	<22.06
9.....	CXOMP J001859.8+162649	00 18 59.83	+16 26 49.3	67.0 ± 10.0	-13.63	-0.64	1.714	44.67	19.92	0.31	0.27	BLAGN	<22.15
10.....	CXOMP J001854.9+162952	00 18 54.92	+16 29 52.8	10.1 ± 4.9	-14.46	-0.68	2.950	44.41	21.78	0.21	-0.14	BLAGN	<22.54

NOTES.—Units of right ascension are hours, minutes, and seconds, and units of declination are degrees, arcminutes, and arcseconds. Table 4 is available in its entirety in the electronic edition of the *Astrophysical Journal Supplement*. A portion is shown here for guidance regarding its form and content.

<sup>a</sup> Observed frame; 2.5–8.0 keV; background subtracted.

<sup>b</sup> Galactic absorption-corrected; observed frame; 2.0–8.0 keV; units of ergs cm<sup>-2</sup> s<sup>-1</sup>.

<sup>c</sup> Rest frame; 2.0–8.0 keV; units of ergs s<sup>-1</sup>.

<sup>d</sup> Source fell near the chip gap. No spectral fitting is performed.

TABLE 5  
 X-RAY SOURCE POPULATIONS

Class	All <sup>a</sup>	$r' < 22.5$	$r' < 22.5; L_x > 10^{42}$ ergs s <sup>-1</sup>
BLAGN.....	139	132	130
NELG.....	53	52	45
ALG.....	18	16	13
STAR.....	10	10	...
Cluster.....	5	5	...
No $z^b$ .....	195	63	...
No opt. <sup>c</sup> .....	82	...	...
Total.....	497 <sup>d</sup>	273	188

<sup>a</sup>  $f_{2.0-8.0\text{ keV}} > 2.7 \times 10^{-15}$  ergs cm<sup>-2</sup> s<sup>-1</sup>.

<sup>b</sup> Optical counterparts with no identification.

<sup>c</sup> No optical counterpart in either  $g'$ ,  $r'$ , or  $i'$ .

<sup>d</sup> Not including clusters that are counted as BLAGNs, NELGs, or ALGs.

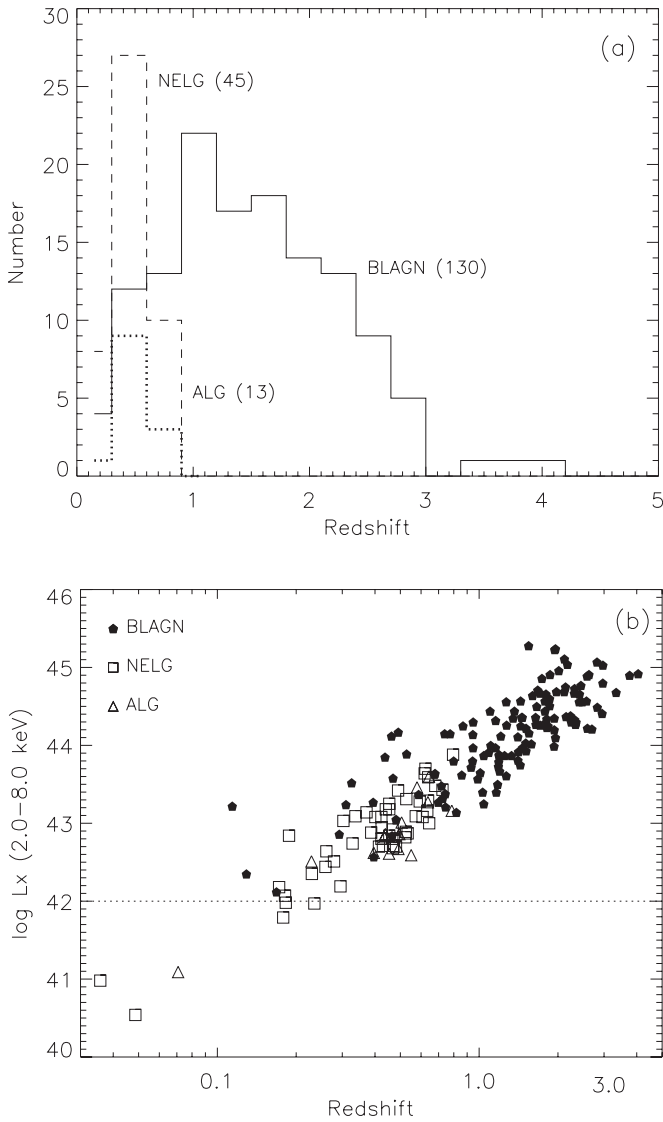


FIG. 3.—(a) Redshift distribution of hard-band-detected AGNs with  $L_{2.0-8.0\text{ keV}} > 10^{42}$  ergs s<sup>-1</sup>. (b) X-ray luminosity, redshift distribution. The horizontal, dashed line marks our chosen minimum luminosity required for AGN selection. All but one NELG [ $z = 0.014$ ;  $\log(L_{2.0-8.0\text{ keV}}) = 39.5$ ] are shown.

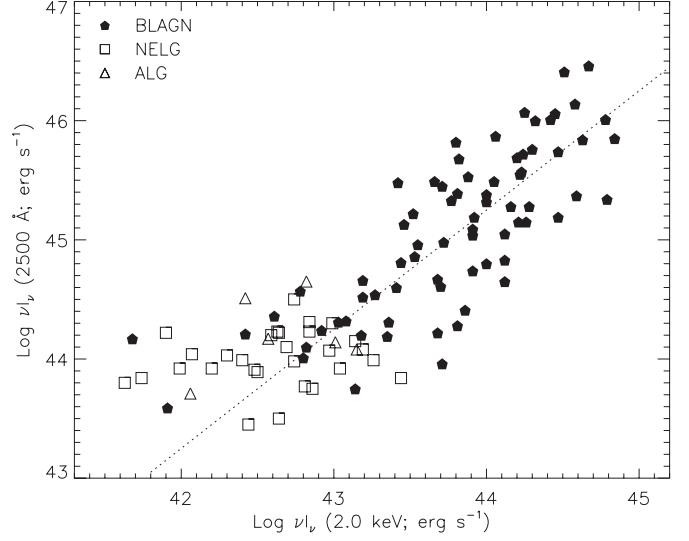


FIG. 4.—X-ray vs. optical luminosity. The dashed line is the mean X-ray-to-optical flux ratio ( $\langle \alpha_{\text{ox}} \rangle = 1.48$ ) of the BLAGNs with  $\log L_{2.0-8.0\text{ keV}} > 43.5$  (units of ergs s<sup>-1</sup>). Propagating typical errors in a Monte Carlo simulation for each object yields error bars of similar size to the points shown here.

#### 6.4. Comparison with the Optically Selected Samples (SDSS)

With optical imaging in three SDSS bands ( $g'$ ,  $r'$ ,  $i'$ ), the SDSS becomes the easiest and largest sample of AGNs to which we can compare our ChaMP AGNs. The second edition of the SDSS quasar catalog (Schneider et al. 2003) contains 16,713 objects with  $M_{i'} < -22$  out to  $z = 5.41$  from the first public data release. We have selected 10,736 of these which were targeted as quasars solely based on their optical colors (BEST spectroscopic  $\text{Cag} = 1$  for either low- $z$  and high- $z$  quasars). In Figure 6a, we have plotted the optical color ( $g' - i'$ ) of the ChaMP AGNs and the quasars from the SDSS as a function of redshift. Following Richards et al. (2001), we have measured the color offset (Fig. 6b) from the median color of type 1 quasars from the SDSS.

The ChaMP BLAGNs follow the color locus of SDSS quasars (Fig. 6) for  $z > 1$ . The ChaMP BLAGNs are slightly redder with a color excess of 0.1 mag compared to the median SDSS quasar colors (Fig. 7). Given the photometric accuracy (0.1 mag) of ChaMP, we cannot with strong confidence report a difference of the mean between the two samples, though we probably achieve a higher precision with our sample of 95 ChaMP BLAGNs. We do find a 0.03% likelihood that the color distribution of the ChaMP BLAGNs ( $z > 1$ ;  $M_{i'} < -22$ ) can be drawn from the SDSS quasar population using a Kolmogorov-Smirnov test (Press et al. 1992). In Figure 7, we see that the ChaMP BLAGNs have a wider color distribution ( $\sigma_{\Delta g'-i'} = 0.41$ ) than the SDSS quasars ( $\sigma_{\Delta g'-i'} = 0.26$ ). Besides the width of the distribution, we can compare the symmetry about the mean by measuring the skewness of the distribution, defined as

$$\text{skewness} = \frac{\sum_{i=1}^N (y_i - \bar{y})^3}{(N-1)\sigma^3}. \quad (2)$$

We find that the distribution of ChaMP BLAGNs has a red wing (skewness  $-1.7$ ) that causes the mean to shift further to the red than the SDSS quasars (skewness 7.1). We calculate that 26% of our ChaMP AGN sample has  $\Delta g' - i' > 0.2$  above that expected from the SDSS distribution. Therefore, an

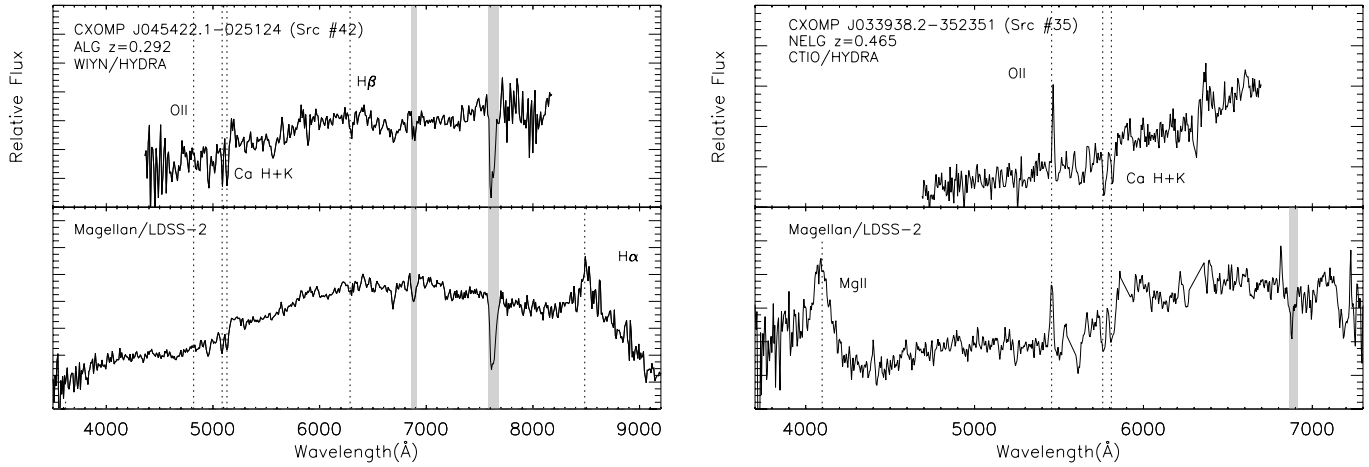


FIG. 5.—Complexity of object classification. Two optical spectra of each source were acquired with slightly different wavelength coverage. The spectra taken with Magellan clearly reveal a broad emission line in each case. Shaded regions mark the uncorrected telluric  $O_2$  absorption features. Dashed lines mark the expected observed wavelengths of emission or absorption features at the source redshift.

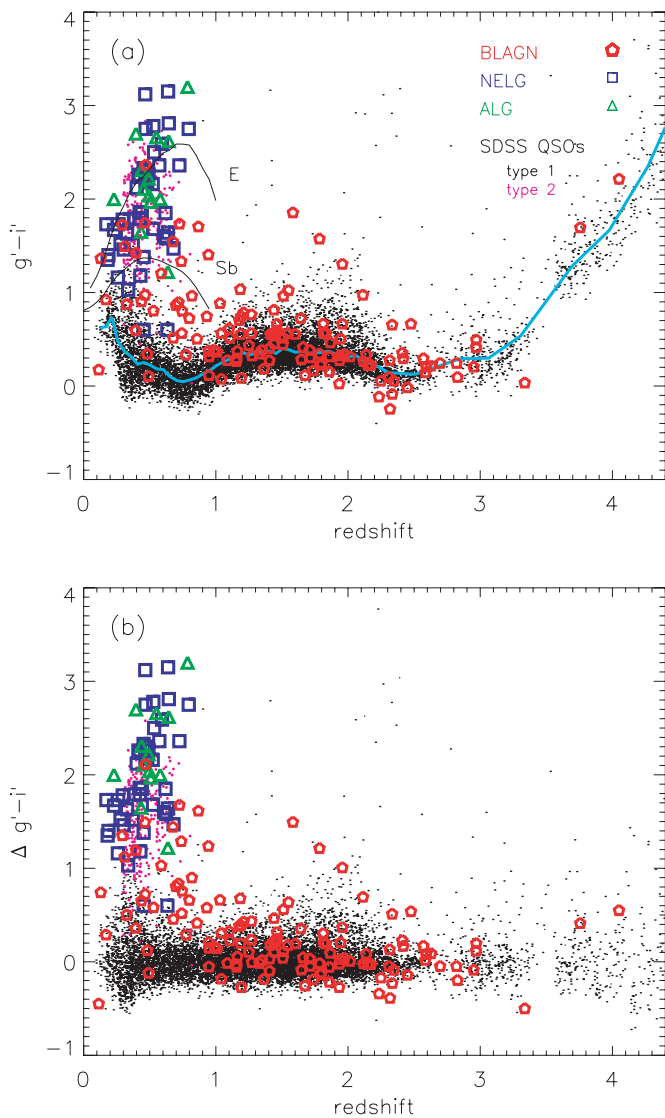


FIG. 6.—(a) Optical color of ChaMP hard AGNs compared with type 1 (Schneider et al. 2003) and type 2 (Zakamska et al. 2003) SDSS quasars. The median type 1 SDSS quasar color in redshift bins of 0.05 ( $z < 2.2$ ), 0.2 ( $2.2 < z < 2.6$ ), and 0.3 ( $z > 2.6$ ) is shown by the cyan curve. (b) Color offsets from the median type 1 quasar color from the SDSS.

X-ray–selected sample can reveal a population of luminous, red AGNs underrepresented in optically selected samples. At  $z < 1$  (Fig. 6), we see a population of red BLAGNs that would not be detected in the SDSS. As shown in Figure 8a, these red BLAGNs tend to have low optical luminosities ( $M_{i'} < -24$ ) and are probably missed in the SDSS because of their continuum color, which can be influenced by their host galaxy. In Figure 8b, we see that many of the red BLAGNs are below the flux limit of the SDSS. A larger sample of optically bright ChaMP AGNs is required to definitively identify a population missed by the optical surveys.

Most ChaMP NELGs and ALGs are red and fall off the color range for optically selected type 1 quasars. We would not expect these types of AGNs to be included in the SDSS quasar catalog owing to their narrow or nonexistent emission lines and most have  $M_{i'} > -22$ . These objects appear to have colors dominated by their host galaxy. To illustrate, we plot in Figure 6a the expected colors of an elliptical (E0) and a spiral (Sb) galaxy using the Hyper\_z (Bolzonella et al. 2000) photometric code.

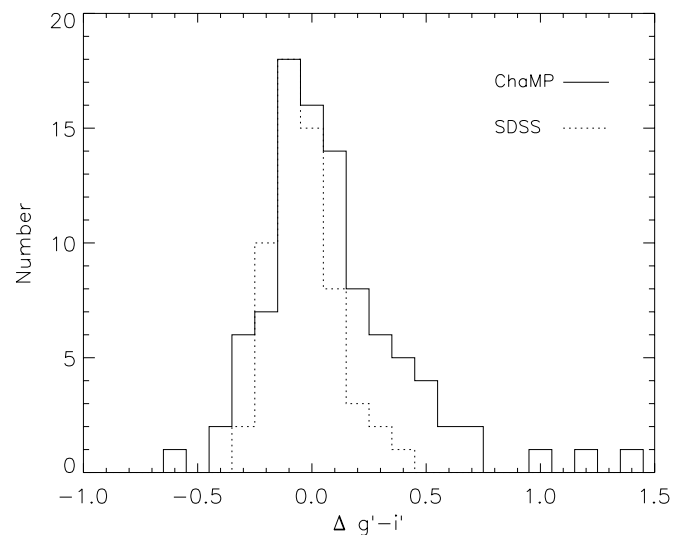


FIG. 7.—Color difference of ChaMP BLAGNs and SDSS quasars with the median SDSS quasar color. A minimum redshift ( $z > 1$ ) has been chosen to omit low-luminosity AGNs with a significant host component. The SDSS distribution has been normalized to match the peak of the ChaMP AGNs.

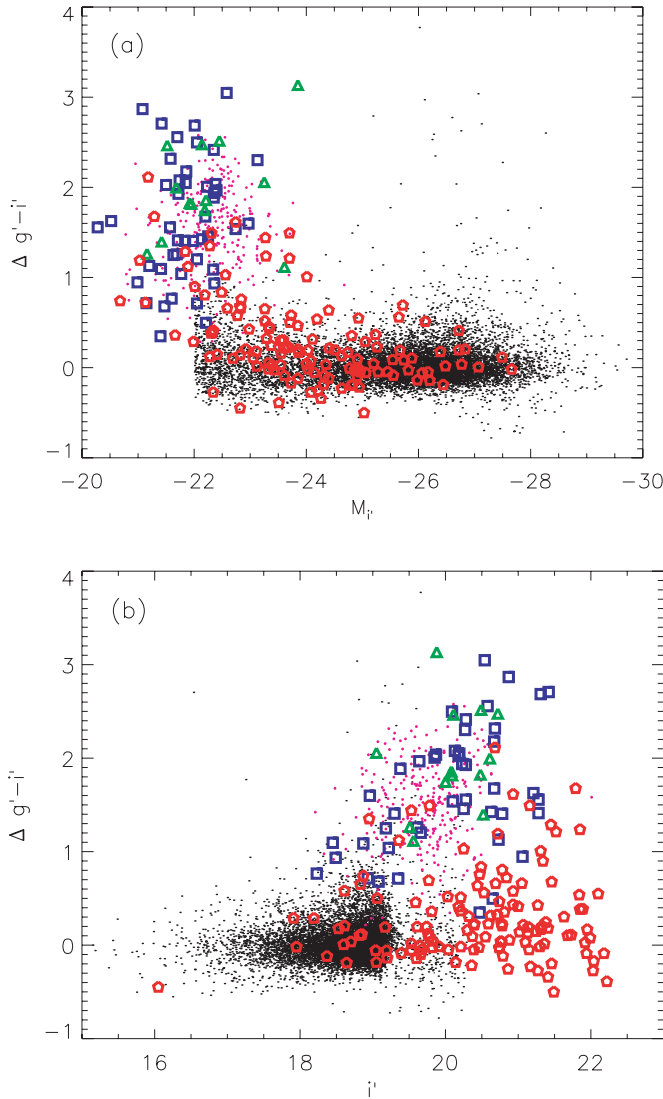


FIG. 8.—Optical color offset as a function of (a) absolute magnitude  $M_V$  and (b) apparent magnitude  $i'$ . Same symbol types as Fig. 6a.

We have assumed a Bruzual-Charlot spectral energy distribution, Galactic extinction ( $E_{B-V} = 0.05$ ) using the Calzetti (1999) reddening law, and no intrinsic dust reddening. Most NELGs and ALGs have colors between these two tracks. We also plot the type 2 SDSS QSO candidates from Zakamska et al. (2003). The absolute magnitude ( $M_V$ ) is calculated from the  $i^*$  magnitude with a correction for Galactic extinction ( $E_{B-V} = 0.05$ ) and no  $k$ -correction. The ChaMP NELGs and SDSS type 2 QSOs potentially represent the same population. The extraordinary advantage of an X-ray-selected survey is seen with the detection of AGNs with no optical emission lines at all (ALGs).

## 7. X-RAY ABSORPTION AND OPTICAL EXTINCTION

We present evidence of a direct relationship between the absorption of X-rays and optical extinction for the majority of the hard AGNs, as expected if unification models (Antonucci 1993) extend to the X-ray regime. We attempt to reconcile the variety of AGN types from an X-ray perspective. We use the term “absorbed” for any AGNs with X-ray  $N_{\text{H}} > 10^{22} \text{ cm}^{-2}$  and “unabsorbed” for those with columns below this value. As justified in § 7.4, this  $N_{\text{H}}$  value represents the amount of absorbing neutral gas needed to hide the broad emission-line

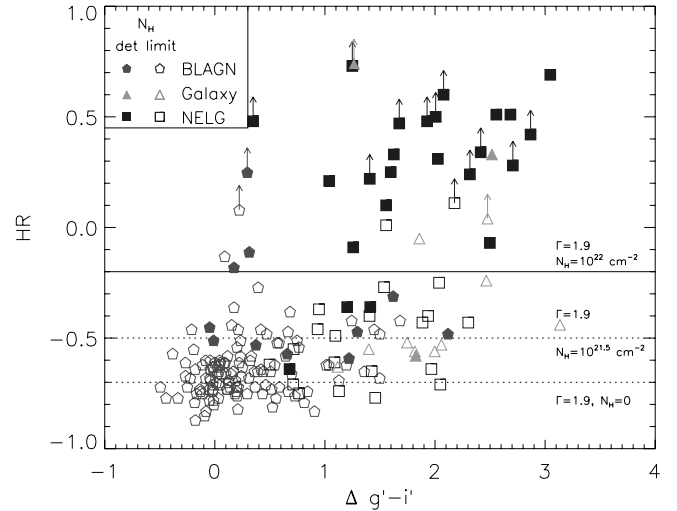


FIG. 9.—Hardness ratio vs. optical color offset. The horizontal lines mark the HR for a typical AGN with a power-law continuum ( $\Gamma = 1.9$ ) absorbed by neutral gas intrinsic to the source. The solid line marks the division between unabsorbed and absorbed AGN as defined in this paper. The filled symbols mark the well-constrained  $N_{\text{H}}$  measurements from X-ray spectral fits (§ 3.1) to compare with Fig. 11. [See the electronic edition of the *Journal* for a color version of this figure.]

region (BLR), assuming a Milky Way gas-to-dust ratio and  $\alpha_{\text{ox}} = 1.48$  for each AGN, in a  $5L_*$  host galaxy. As discussed below, most AGNs with unabsorbed X-ray emission show signs of optical emission from the BLR. Alternatively, judging by the lack of broad emission lines, most X-ray absorbed AGNs have significant optical extinction. However, there is a small though significant fraction that do not fall into the simple obscured or unobscured scenario. The various classes illustrating the permutations of X-ray absorption and optical extinction are delineated in the following sections.

### 7.1. Unabsorbed AGNs with Broad Emission Lines

We find that the majority of AGNs with unabsorbed ( $N_{\text{H}} < 10^{22} \text{ cm}^{-2}$ ) X-ray emission have no apparent extinction of their optical light. First, the optical spectra of 80% of the unabsorbed AGNs (HR < -0.2; Fig. 2) are characterized by the presence of broad emission lines (e.g., Ly $\alpha$ , C IV, C III], Mg II). In Figure 9, we plot the X-ray hardness ratio as a function of optical color offset (§ 6.4) for our AGN sample. These BLAGNs have blue optical colors and are grouped in a region (HR < -0.4 and  $\Delta g' - i' < 1$ ) characteristic of unobscured AGNs. As mentioned previously, our BLAGN sample at  $z > 1$  has colors similar to the optically selected SDSS quasars (Fig. 6a) but with a slightly broader and skewed distribution (Fig. 7). We conclude that no significant obscuring material is preventing us from observing the broad-line region in these unabsorbed AGNs.

We find that 10% of ChaMP BLAGNs have red optical colors with  $\Delta g' - i' > 1.0$  (Fig. 9), offset from the locus of SDSS quasars (Fig. 6a). We suspect that host galaxy emission is contributing to their red optical color since these ChaMP BLAGNs, mostly at  $z < 1$ , represent the lower luminosity fraction of our sample ( $L_{2-8 \text{ keV}} < 10^{44} \text{ ergs s}^{-1}$ ; Fig. 3). To further illustrate, Figure 8a shows that the absolute magnitudes ( $M_V$ ) and colors of these red BLAGNs are intermediate between the non-BLAGNs and the more luminous ( $M_V$ ) AGNs. We present in Figure 5, optical spectra of two such objects with composite (AGN+host) spectra. Both of these AGNs have broad optical emission lines but their red optical continuum is dominated

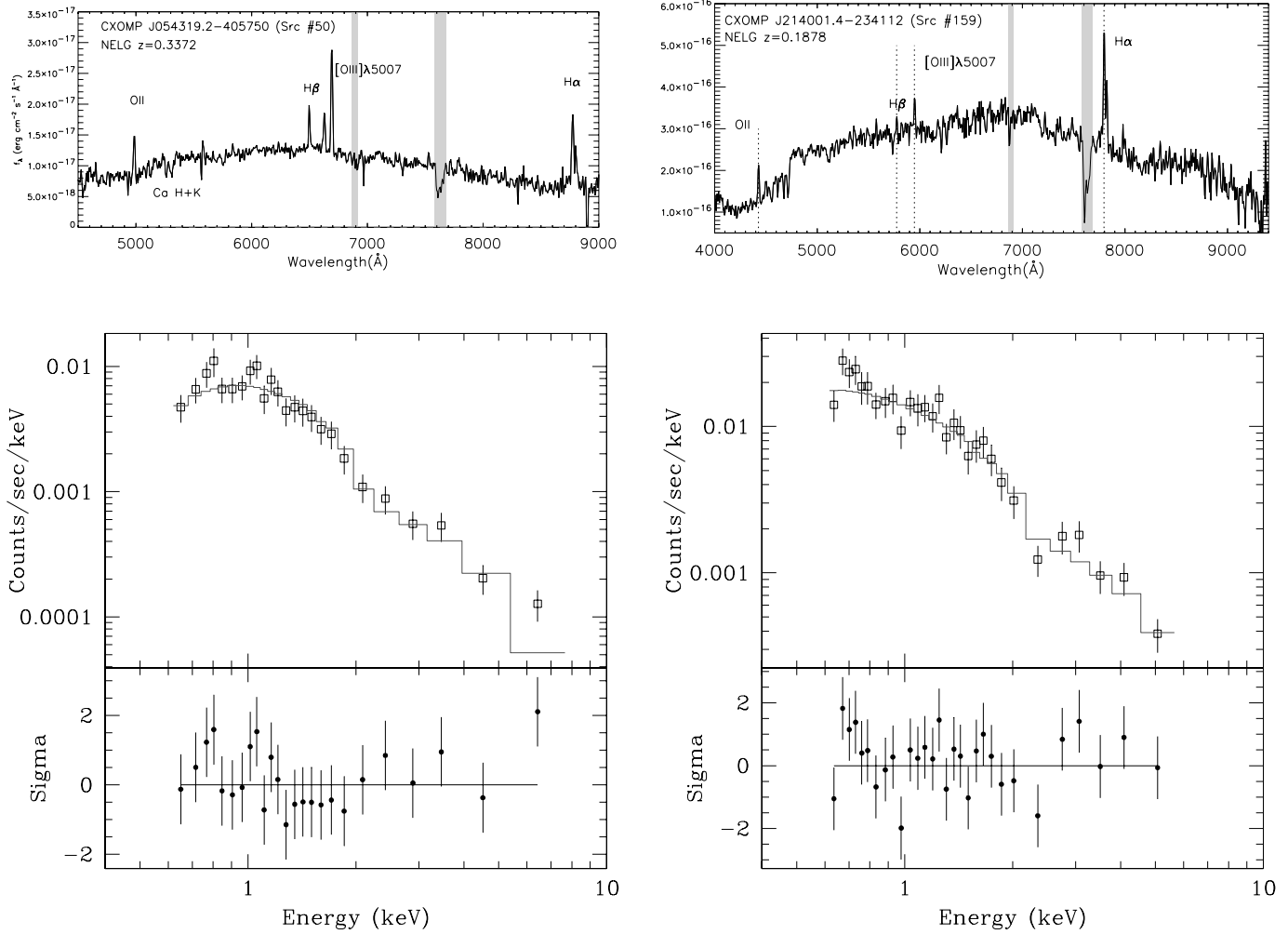


FIG. 10.—X-ray and optical spectra of two X-ray unabsorbed, narrow emission-line galaxies. Each column corresponds to one source. (*Top row*) Optical spectra, with shaded regions to mark the uncorrected atmospheric absorption features, are displayed. (*Bottom row*) Best-fit absorbed power-law model (*top*) and residuals (*bottom*) are shown for each object.

by the host galaxy. Extinction due to dust might contribute to both their low luminosity and optical color. Dust extinction is probably responsible for the red colors of three luminous ( $L_{2-8\text{ keV}} > 10^{44}$  ergs  $\text{s}^{-1}$ ) BLAGNs seen in Figure 6a with  $1.5 < z < 2.0$ . The ChaMP BLAGNs might be a fainter version of the 2MASS selected, red, and X-ray unabsorbed BLAGNs (Wilkes et al. 2002).

### 7.2. Unabsorbed AGNs Lacking Broad Emission Lines

Surprisingly, a number of unabsorbed AGNs show no broad optical emission lines. These objects are clearly seen in Figure 9 with  $\text{HR} < -0.2$  and  $\Delta g' - i' > 1.0$ . The nature of these sources is the least understood. Their red optical colors are characteristic of their host galaxy, but the classification might be due to the fact that at certain redshifts, we lose the AGN diagnostic emission lines (e.g.,  $\text{H}\alpha$ ,  $\text{Mg II}$ ) within the observed optical spectroscopic window for sources with comparable host galaxy and AGN optical emission as discussed in § 6.3. Usually  $\text{H}\beta$  is the only line available, which can suffer from both extinction and contamination due to the host galaxy. We are pursuing spectroscopy further to the red for some of these objects to detect  $\text{H}\alpha$  for emission-line diagnostics to securely identify the ionizing source as either an AGN or starburst. Many of these AGNs are at  $z > 0.4$  with  $\text{H}\alpha$  at  $\lambda > 9200$  Å, making this type of analysis difficult for optically faint AGNs.

Two bright NELGs may provide insight into the nature of this class of unabsorbed AGNs ( $N_{\text{H}} < 10^{22}$   $\text{cm}^{-2}$ ). These objects might be similar to the rare unabsorbed Seyfert 2 galaxies seen by other groups in nearby objects (Georgantopoulos & Zezas 2003; Panessa & Bassani 2002). With over 400 counts in both sources [CXOMP J054319.2–405750 (source 50;  $\log L_{\text{X}} = 43.05$ ;  $M_{\text{E}} = -22.05$ ), CXOMP J214001.4–234112 (source 159;  $\log L_{\text{X}} = 43.08$ ;  $M_{\text{E}} = -22.35$ )], we are able to constrain their X-ray spectral properties. We fit the data using a spectral model with the photon index and the intrinsic absorption as free parameters (see § 3.1). Figure 10 shows the X-ray and optical spectra. Source 50 is very soft with  $\Gamma = 2.29^{+0.22}_{-0.16}$  and  $N_{\text{H}} < 8.2 \times 10^{20}$   $\text{cm}^{-2}$ . There could possibly be a soft excess below 2 keV. Source 159 has a photon index  $\Gamma = 1.83^{+0.21}_{-0.13}$  with  $N_{\text{H}} < 7.6 \times 10^{20}$   $\text{cm}^{-2}$ . These AGNs show no signs of X-ray absorption, while their optical spectra show a strong galaxy continuum with overlying narrow emission lines. The width of  $\text{H}\beta$  is 323  $\text{km s}^{-1}$  in source 50 and the width of  $\text{H}\alpha$  is 669  $\text{km s}^{-1}$  in source 159. Surprisingly, their low-ionization emission-line ratios are not typical of an AGN, but resemble those of a star-forming galaxy. We can explain the X-ray and optical properties with any of the following scenarios: (1) severe dilution of the AGN emission by a host undergoing prodigious star formation, (2) a Compton thick obscuring medium in which we observe the indirect, reflected component of the X-ray

emission and the optical light is purely from the host galaxy owing to severe dust extinction, (3) a high dust-to-neutral gas ratio, which allows only the X-rays to penetrate, or (4) beamed emission from a BL Lac. To properly discriminate between these models, a sample of nearby AGNs for which we can resolve the nuclear region and properly subtract the host emission would be ideal. For the Compton thick case, the true  $L_x$  may be much higher. In addition, we may find a large  $L_{\text{IR}}$  from reprocessed emission.

We are finding a population of optically “dull” galaxies (Severgnini et al. 2003; Silverman et al. 1998; Tananbaum et al. 1997; Elvis et al. 1981), recently coined XBONGS (Comastri et al. 2002). These are galaxies with X-ray-bright nuclei that have weak or nonexistent emission lines. All but a couple of the 13 ALGs identified in this study are not heavily absorbed (Fig. 9). Similar X-ray properties have been noted in recent studies of other examples (e.g., Severgnini et al. 2003). As shown in Figure 5, we may be able to detect AGN optical signatures in some of these ALGs using expanded wavelength coverage to include  $H\alpha$ , which is less susceptible to dust extinction and stellar absorption features. Using the definition of Dressler & Shechtman (1987), only two are possible BL Lac candidates based upon their 4000 Å break contrast.

### 7.3. Absorbed AGNs

We find that most X-ray-absorbed ( $N_{\text{H}} > 10^{22} \text{ cm}^{-2}$ ) AGNs suffer from optical extinction. Almost all of the AGNs (84%) with  $\text{HR} > -0.2$ , lack broad optical emission lines (Fig. 9). These absorbed AGNs tend to have narrow emission lines in their optical spectra. At these redshifts ( $z > 0.4$ ), the optical spectra rarely include a detection of all the emission lines ( $H\alpha$ ,  $N \text{ II}$ ,  $[\text{O III}]$ ,  $H\beta$ ) needed to solidify the optical classification as an AGN as opposed to a star-forming galaxy. Given their high X-ray luminosity ( $L_x > 10^{42} \text{ ergs s}^{-1}$ ), we are confident that the X-ray emission is due to supermassive black hole accretion.

In Figure 9, we show that these absorbed AGNs ( $\text{HR} > -0.2$ ) have red optical colors ( $\Delta g' - i' > 1.5$ ) characteristic of their host galaxy and not the AGN itself (Green et al. 2004; Fiore et al. 2003). Most of these AGNs have colors offset from the locus of optically selected QSOs and fall along the track of an early-type galaxy as shown in Figure 6a. These results agree with studies that conclude that AGNs are predominantly found in massive, early-type galaxies (Kauffmann et al. 2003). For the most part, AGNs which suffer from absorption in the X-rays have significant optical extinction that hides emission from the BLR.

### 7.4. Intrinsic $N_{\text{H}}$

We have measured the amount of intrinsic absorption toward each AGN by fitting the X-ray count distribution with a fixed power-law model as described in § 3.1. In Figure 11, we plot the best-fit intrinsic  $N_{\text{H}}$  as a function of rest-frame X-ray luminosity. Measurements with errors ( $1.6 \sigma$ ) are plotted as filled symbols. Upper limits are marked as hollow symbols placed at the  $1.6 \sigma$  upper limit with a downward arrow.

The absorbed AGNs have columns in the range of  $10^{22} \text{ cm}^{-2} < N_{\text{H}} < 10^{24} \text{ cm}^{-2}$ . The majority of these are optically classified as NELGs. We have uncovered five luminous AGNs with  $L_{2-8 \text{ keV}} > 10^{44} \text{ ergs s}^{-1}$  that are heavily absorbed with well-constrained columns ( $N_{\text{H}} > 10^{22} \text{ cm}^{-2}$ ). These quasars would not be singled out as having high absorption based on their hardness ratios since they are mostly at  $z > 1.7$ , where the observed X-ray counts are less affected by absorp-

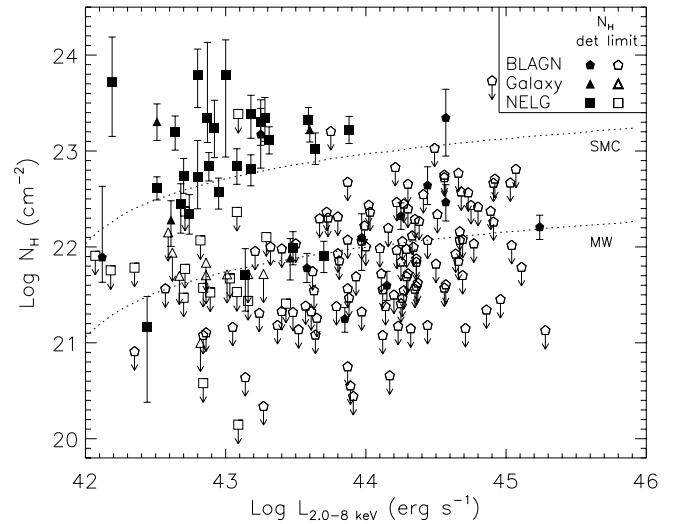


FIG. 11.—Luminosity vs.  $N_{\text{H}}$ . The X-ray luminosity has only been corrected for Galactic absorption. Error bars represent 90% confidence intervals. The filled symbols mark the well-constrained  $N_{\text{H}}$  measurements. Upper limits are shown with hollow symbols placed at the 90% value. The dashed lines mark our estimate of the absorbing column needed to hide optical emission from the broad-line region for a given X-ray luminosity, assuming the average dust-to-gas ratio from Pei (1992) of the Milky Way (MW) and Small Magellanic Cloud (SMC). [See the electronic edition of the *Journal* for a color version of this figure.]

tion. (In Fig. 9, the BLAGNs with well-constrained values of  $N_{\text{H}}$  [filled symbols] do not necessarily have  $\text{HR} > -0.2$ .) While these quasars have broad emission lines in their optical spectra (Fig. 12), they all show signs of either absorption or extinction in the optical. Two sources (Figs. 12a and 12d) have a reddened optical continuum possibly attributed to dust extinction and similar to the red quasar 3C 212 (Elvis et al. 1994). Their colors are substantially offset from the SDSS quasar locus in Figure 6. Three (Figs. 12b, 12c, and 12d) have narrow absorption lines that might be related to the X-ray absorption. Source CXOMP J230240.2+083611 (source 176 in Fig. 12b) has an absorption line blueshifted from the emission line center. This is evidence for ionized intrinsic outflows, which are known to have high absorbing gas columns ( $N_{\text{H}} \sim 6 \times 10^{22} \text{ cm}^{-2}$ ) in BALQSOs (Green et al. 2001). Even in non-BALQSOs, Laor & Brandt (2002) found an association in quasars between (soft) X-ray weakness and C IV absorption equivalent width. While the spectrum of source CXOMP J230211.1+084657 (source 173, Fig. 12e) has a poor S/N ratio, absorption might be seen blueward of the C IV emission line. The object CXOMP J134450.6+555531 (source 113 in Fig. 12c) has narrow absorption lines detached from the emission lines. Either these absorption lines are extremely fast outflows intrinsic to the AGNs or a more probable explanation is an intervening absorber. Based on these five absorbed quasars, we find that 6% (5/79) of luminous ( $L_{2-8 \text{ keV}} > 10^{44} \text{ ergs s}^{-1}$ ) X-ray-selected BLAGNs have  $N_{\text{H}} > 10^{22} \text{ cm}^{-2}$  (2% of all AGNs). This is consistent with the value of 10% found by Perola et al. (2004) and Page et al. (2003).

As expected, the unabsorbed ( $N_{\text{H}} < 10^{22} \text{ cm}^{-2}$ ; Fig. 11) AGN population is dominated by BLAGNs. Almost all of the measurements are poorly constrained (upper limits) with a low probability of significant absorption. The apparent trend of increasing  $N_{\text{H}}$  with luminosity for the BLAGNs is probably due to our decreasing sensitivity to the absorbing column at higher redshifts, rest-frame soft X-rays, most susceptible to absorption, are redshifted out of the *Chandra* bandpass. There

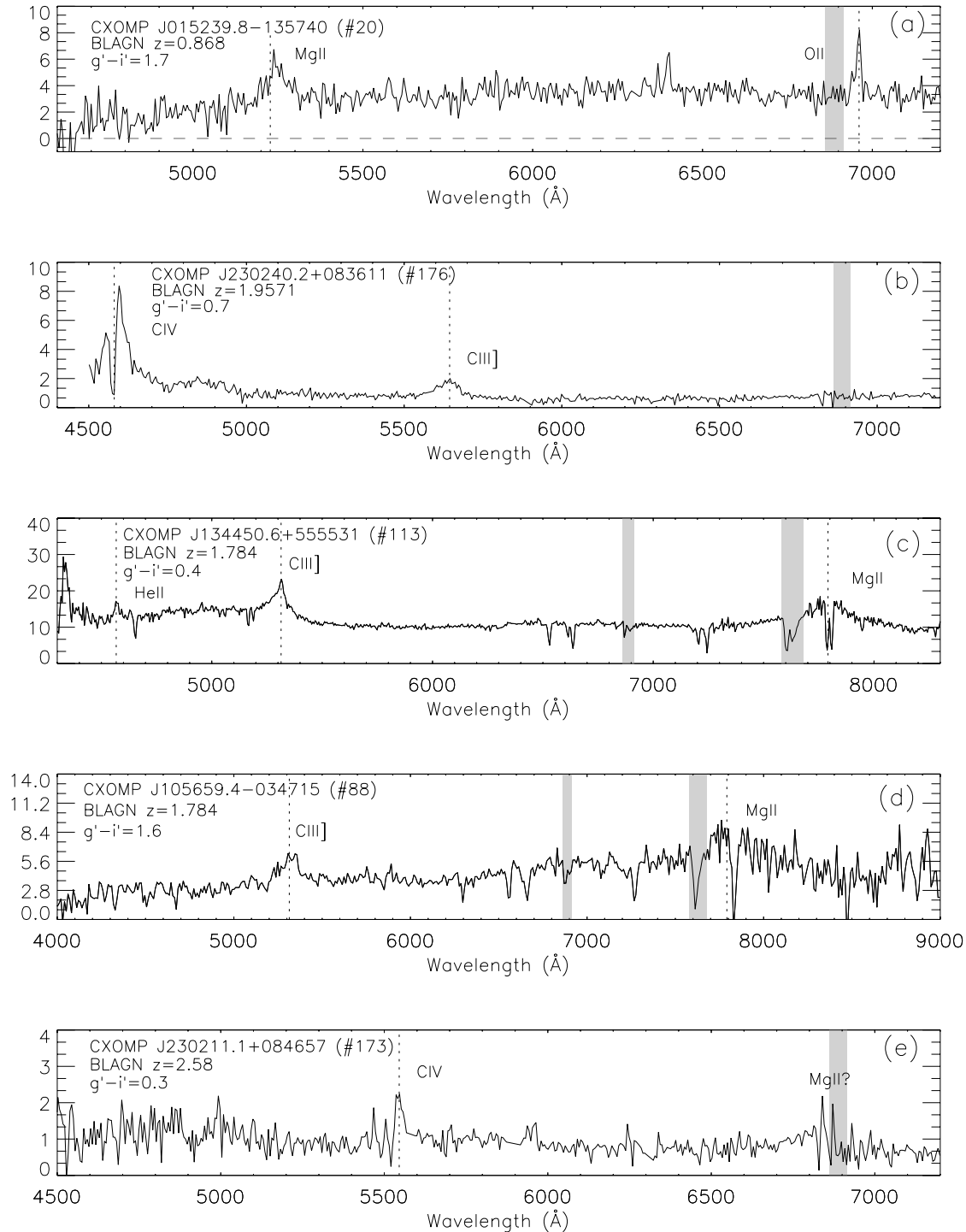


FIG. 12.—Optical spectra of X-ray-absorbed quasars with  $N_{\text{H}} > 10^{22} \text{ cm}^{-2}$  and rest frame  $L_{2-8 \text{ keV}} > 10^{44} \text{ ergs s}^{-1}$ . The flux ( $f_i$ ; y-axis) is in units of  $10^{-17} \text{ ergs cm}^{-2} \text{ s}^{-1} \text{ \AA}^{-1}$ . Dashed lines show the spectral features at the redshift of the object. The optical color ( $g' - i'$ ) is given. Shaded regions mark the uncorrected telluric O<sub>2</sub> absorption bands.

are a fair number of NELGs and ALGs with no measurable absorbing column. As described in the previous section, we suspect that host dilution is confusing the spectroscopic characterization of these sources.

We crudely estimate the  $N_{\text{H}}$  needed to hide the optical emission from an embedded AGN of a given X-ray luminosity. From the rest-frame  $L_{2.0-8.0 \text{ keV}}$  and  $\alpha_{\text{OX}} = 1.48$  (the mean X-ray-to-optical flux ratio for the X-ray-selected BLAGNs; § 6.3), we calculate the expected unabsorbed  $l_{\nu}$  (2500 Å). We then compare the 2500 Å monochromatic luminosity to that of a host

galaxy, assuming  $L_{\text{Host}} = 5L_*$ . This luminosity corresponds to the average host absolute magnitude ( $M_B = -23.0$ ) found by Jahnke & Wisotzki (2003) for a sample of bright QSOs. Using the gas-to-dust ratio of the Milky Way ( $N_{\text{H}} = 4.82 \times 10^{21} E_{B-V} \text{ mag}^{-1} \text{ cm}^{-2}$ ) and Small Magellanic Cloud ( $N_{\text{H}} = 4.52 \times 10^{22} E_{B-V} \text{ mag}^{-1} \text{ cm}^{-2}$ ) from Pei (1992), we determine the amount of dust extinction and hence the column density required to diminish the AGN optical light to a tenth of the assumed host optical luminosity. The dashed lines in Figure 11 shows the results from this rather simplified calculation for both gas-to-dust

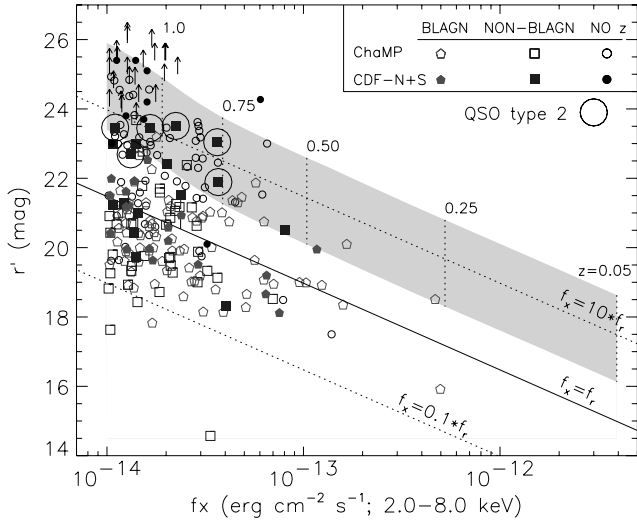


FIG. 13.—Where are the type 2 QSOs? The shaded region marks the location of a hypothetical, obscured QSO out to  $z = 1.45$  as described in § 7.5. We have included the sources from the *Chandra* Deep Fields, which include six such quasars. [See the electronic edition of the *Journal* for a color version of this figure.]

ratios. Based on the gas-to-dust ratio of the Milky Way, the column densities needed to hide an AGN are  $N_{\text{H}} \sim 10^{22} \text{ cm}^{-2}$ , which marks our division between absorbed and unabsorbed AGNs. The column densities could potentially be higher (Fig. 11; *top*, *dashed line*), given that luminous quasars found in the SDSS have dust extinction more typical of the Small Magellanic Cloud (Hopkins et al. 2004).

#### 7.5. Optically Faint X-Ray Sources and Type 2 Quasars

As evident from Figure 1, there are many unidentified X-ray sources with  $r' > 22$ . We believe that a significant fraction of these sources may be the elusive type 2 quasars.

A number of ongoing X-ray surveys (e.g., CDF-N and CDF-S) have acquired spectroscopic redshifts fainter than the current ChaMP sample and have identified a few as luminous narrow-line AGNs. The HELLAS2XMM (Fiore et al. 2003) survey has spectroscopically identified 8 type 2 QSOs from a sample of 13 over  $0.9 \text{ deg}^2$  with  $f_{\text{x}}/f_{\text{r}} > 10$ . The redshift range of these quasars ( $0.7 < z < 1.8$ ) as described previously has been inaccessible to ChaMP (Fig. 3) because of our bright spectroscopic limit.

To investigate the lack of obscured, highly luminous quasars in our sample, we illustrate their expected location in  $f_{\text{x}} - r'$  space (Fig. 13). We plot only the X-ray-bright ( $f_{2-8 \text{ keV}} > 1 \times 10^{-14} \text{ ergs cm}^{-2} \text{ s}^{-1}$ ) extragalactic sources (with the exclusion of clusters) and the unidentified objects. We have shaded the region for a hypothetical quasar with  $L_{\text{X}} = 10^{44} \text{ ergs s}^{-1}$  and optical emission purely from a host elliptical galaxy ( $L_{*} < L_{\text{r}} < 10L_{*}$ ) using Hyper\_z (Bolzonella et al. 2000). We have labeled the redshifts ( $0.05 < z < 1.0$ ) in this region with dashed vertical lines. We infer that most obscured quasars probably fall within the region with  $r' > 22$  based on our X-ray sensitivity and area coverage.

To test this hypothesis, we have included data from the CDF-N and CDF-S, which have detected six type 2 quasars with  $f_{\text{x}} > 1 \times 10^{-14} \text{ ergs cm}^{-2} \text{ s}^{-1}$ ,  $L_{2-8 \text{ keV}} > 10^{44} \text{ ergs s}^{-1}$  and no evidence for any broad optical emission lines. The optical magnitudes of these sources have been converted to the SDSS photometric system using the transformations in Fukugita et al.

(1996). For the CDF-S data, we use average colors for each object class from the CDF-N sources to convert the *R*-band magnitude (Szokoly et al. 2003). It is apparent from the six possible type 2 quasars in the deep fields that there is potentially a significant number of obscured quasars yet to be identified at faint optical magnitudes.

The optically undetected, X-ray-bright objects must await infrared follow-up to learn more about their source properties. However, we can look at the X-ray hardness ratios to infer their host optical properties. From Figure 2, we see that the optically undetected sources have a wide range of hardness ratio with many extreme cases ( $\text{HR} > 0$ ). Since these X-ray sources have a HR distribution most similar to the NELGs at  $f_{\text{x}} > 1 \times 10^{-14} \text{ ergs cm}^{-2} \text{ s}^{-1}$ , it seems likely that many of these optically undetected sources are the narrow emission-line objects at higher redshift possibly comprising a significant fraction of the highly luminous and obscured quasar population.

## 8. CONCLUSIONS

We have presented an analysis of the X-ray and optical properties of 188 hard X-ray-selected AGNs in 20 medium depth ChaMP fields. These AGNs have been classified by optical spectroscopy to be comprised of BLAGNs (69%), NELGs (24%), or ALGs (7%). Overall, we find that 81% of the AGNs agree with simple AGN unification models (Antonucci 1993). The two main points of evidence are as follows:

1. 80% of unabsorbed AGNs ( $N_{\text{H}} < 10^{22} \text{ cm}^{-2}$ ) have optical properties characterized by broad emission lines. The optical colors of ChaMP BLAGNs are predominately blue ( $g' - i' < 1.0$ ) and similar to optically selected quasars from the SDSS but with a slightly wider distribution. A significant red ( $g' - i' > 1.0$ ) BLAGN population exists with optical properties influenced by their host galaxy. These objects represent 10% of the full AGN sample.
2. 84% of absorbed AGNs ( $N_{\text{H}} > 10^{22} \text{ cm}^{-2}$ ) lack broad optical emission lines. Most are associated with NELGs with column densities in the range  $10^{22} \text{ cm}^{-2} < N_{\text{H}} < 10^{24} \text{ cm}^{-2}$ . Their optical colors ( $g' - i' > 1.0$ ) are characteristic of a luminous, early-type galaxy.

We also find a number of atypical AGNs (19%) whose X-ray and optical properties can be explained without any need to alter the AGN unification models:

1. The lack of broad optical emission lines in X-ray unabsorbed, NELGs and ALGs can be attributed to a strong host galaxy contribution in 17% of the total AGN sample.
2. The large amount of X-ray absorption ( $N_{\text{H}} > 10^{22} \text{ cm}^{-2}$ ) in a few BLAGNs (2% of all AGNs) may be related to signatures of absorption in their optical spectra. A future ChaMP study will determine if the X-ray absorption is associated with warm (ionized) intrinsic outflowing gas similar to that seen in broad absorption line quasars.

We are greatly indebted to NOAO and the SAO TAC for their support of this work. Many thanks to Robert Kirshner, Warren Brown, John Huchra, Kevin Krisciunas, and Guillermo Torres for contributing to the ChaMP spectroscopic program. We remain indebted to the staffs at Kitt Peak, CTIO, Las Campanas, Keck, FLWO, and MMT for assistance with optical observations.

We gratefully acknowledge support for this project under NASA under CXC archival research grants AR3-4018X and AR4-5017X. T. L. Aldcroft, W. A. Barkhouse, R. A. Cameron, P. J. Green, D. W. Kim, A. E. Mossman, H. Tananbaum, and

B. Wilkes also acknowledge support through NASA contract NASA contract NAS8-39073 (CXC). D. Wik receives support through the SAO Research Experiences for Undergraduates (REU) Summer Intern Program that is supported by the NSF.

## REFERENCES

- Akylas, A., Georgantopoulos, I., & Barcons, X. 2003, *A&A*, 403, 869
- Antonucci, R. R. J. 1993, *ARA&A*, 31, 473
- Antonucci, R. R. J., & Miller, J. S. 1985, *ApJ*, 297, 621
- Barcons, X., Carrera, F. J., Ceballos, M. T., Mateos, S., Page, M. J., Pérez-Fourmon, I., & Watson, M. G. 2003, *Astron. Nachr.*, 324, 44
- Barger, A. J., Cowie, L. L., Brandt, W. N., Capak, P., Garmire, G. P., Hornschemeier, A. E., Steffen, A. T., & Wehner, E. H. 2002, *AJ*, 124, 1839
- Barger, A. J., Cowie, L. L., Capak, P., Alexander, D. M., Bauer, F. E., Fernandez, E., Brandt, W. N., & Garmire, G. P. 2003, *AJ*, 126, 632
- Bertin, E., & Arnouts, S. 1996, *A&AS*, 117, 393
- Bolzonella, M., Miralles, J.-M., & Pelló, R. 2000, *A&A*, 363, 476
- Calzetti, D. 1999, *Ap&SS*, 266, 243
- Comastri, A., Setti, G., Zamorani, G., & Hasinger, G. 1995, *A&A*, 296, 1
- Comastri, A., et al. 2002, *ApJ*, 571, 771
- Cowie, L. L., Barger, A. J., Bautz, M. W., Brandt, W. N., & Garmire, G. P. 2003, *ApJ*, 584, L57
- Cowie, L. L., Garmire, G. P., Bautz, M. W., Barger, A. J., Brandt, W. N., & Hornschemeier, A. E. 2002, *ApJ*, 566, L5
- Dickey, J. M., & Lockman, F. J. 1990, *ARA&A*, 28, 215
- Dressler, A., & Shechtman, S. 1987, *AJ*, 94, 899
- Elvis, M., Fabrizio, F., Mathur, S., & Wilkes, B. J. 1994, *ApJ*, 425, 103
- Elvis, M., Schreier, E. J., Tonry, J., Davis, M., & Huchra, J. P. 1981, *ApJ*, 246, 20
- Fiore, F., et al. 2003, *A&A*, 409, 79
- Freeman, P. E., Kashyap, V., Rosner, R., & Lamb, D. Q. 2002, *ApJS*, 138, 185
- Fukugita, M., Ichikawa, T., Gunn, J. E., Doi, M., Shimasaku, K., & Schneider, D. P. 1996, *AJ*, 111, 1748
- Georgantopoulos, I., & Zezas, A. 2003, *ApJ*, 594, 704
- Gilli, R., Salvati, M., & Hasinger, G. 2001, *A&A*, 366, 407
- Green, P. J., Aldcroft, T. L., Mathur, S., Wilkes, B., & Elvis, M. 2001, *ApJ*, 558, 109
- Green, P. J., et al. 2004, *ApJS*, 150, 43
- Hasinger, G., Burg, R., Giacconi, R., Schmidt, M., Trumper, J., & Zamorani, G. 1998, *A&A*, 329, 482
- Hasinger, G., et al. 2001, *A&A*, 365, 45
- Harrison, F. A., Eckart, M. E., Mao, P. H., Helfand, D. J., & Stern, D. 2003, *ApJ*, 596, 944
- Ho, L. C., Filippenko, A. V., Sargent, W. L., & Peng, C. Y. 1997, *ApJS*, 112, 391
- Hopkins, P. F., et al. 2004, preprint (astro-ph/0406293)
- Jahnke, K., & Wisotzki, L. 2003, *MNRAS*, 346, 304
- Kauffmann, G., et al. 2003, *MNRAS*, 346, 1055
- Kim, D.-W., et al. 2004a, *ApJS*, 150, 19
- Kim, D.-W., et al. 2004b, *ApJ*, 600, 59
- Laor, A., & Brandt, W. N. 2002, *ApJ*, 569, L641
- Lira, P., Ward, M., Zezas, A., Alonso-Herrero, A., & Ueno, S. 2002, *MNRAS*, 330, 259
- Mainieri, V., Bergeron, J., Hasinger, G., Lehmann, I., Rosati, P., Schmidt, M., Szokoly, G., & Della Cecca, R. 2002, *A&A*, 393, 425
- Moran, E. C., Filippenko, A. V., & Chornock, R. 2002, *ApJ*, 579, L71
- Moretti, A., Campana, S., Lazzati, D., & Tagliaferri, G. 2003, *ApJ*, 588, 696
- Mushotzky, R. F., Cowie, L. L., Barger, A. J., & Arnaud, K. A. 2000, *Nature*, 404, 459
- O'Sullivan, E., Forbes, D. A., & Ponman, T. J. 2001, *MNRAS*, 328, 461
- Page, M. J., et al. 2003, *Astron. Nachr.*, 324, 101
- Panessa, F., & Bassani, L. 2002, *A&A*, 394, 435
- Pei, Y. C. 1992, *ApJ*, 395, 130
- Perola, G. C., et al. 2004, preprint (astro-ph/0404044)
- Piconcelli, E., Cappi, M., Bassani, L., Di Cocco, G., & Dadina, M. 2003, *A&A*, 412, 689
- Press, W. H., Teukolsky, S. A., Vetterling, W. T., & Flannery, B. P. 1992, *Numerical Recipes in C: The Art of Scientific Computing* (Cambridge: Cambridge Univ. Press)
- Reeves, J. N., & Turner, M. J. L. 2000, *MNRAS*, 316, 234
- Richards, G. T., et al. 2001, *AJ*, 121, 2308
- Schlegel, E. M., & Salinas, A. 2004, in *ASP Conf. Ser., Magnetic Cataclysmic Variables*, ed. M. Cropper & S. Vrielmann (San Francisco: ASP), in press
- Schneider, D. P., et al. 2003, *AJ*, 126, 2579
- Severgnini, P., et al. 2003, *A&A*, 406, 483
- Silverman, J. D., Harris, D. E., & Junor, W. 1998, *A&A*, 335, 443
- Smith, D. A., & Done, C. 1996, *MNRAS*, 280, 355
- Stoche, J. T., Morris, S. L., Gioia, I. M., Maccacaro, T., Schild, R., Wolter, A., Fleming, T. A., & Henry, J. P. 1991, *ApJS*, 76, 813
- Szokoly, G. P., et al. 2003, preprint (astro-ph/0312324)
- Tananbaum, H., Tucker, W., Prestwich, A., & Remillard, R. 1997, *ApJ*, 476, 83
- Tozzi, P., et al. 2001, *ApJ*, 562, 42
- Turner, T. J., George, I. M., Nandra, K., & Mushotzky, R. F. 1997, *ApJ*, 488, 164
- Valdes, F. G. 2002, in *Automated Data Analysis in Astronomy*, ed. R. Gupta, H. P. Singh, & C. A. L. Bailer-Jones (New Delhi: Narosa Publ. House), 309
- Wilkes, B. J., Schmidt, G. D., Cutri, R. M., Ghosh, H., Hines, D., Nelson, B., & Smith, P. S. 2002, *ApJ*, 564, L65
- Yuan, W., Brinkmann, W., Siebert, J., & Voges, W. 1998, *A&A*, 330, 108
- Zakamska, N. L., et al. 2003, *AJ*, 126, 2125
- Zezas, A., Ward, M. J., & Murray, S. S. 2003, *ApJ*, 594, L31